The Planetary Science Journal, 7:27 (18pp), 2026 February https://doi.org/10.3847/PSJ/ae2fb9
© 2026. The Author(s). Published by the American Astronomical Society.
OPEN ACCESS

Spectral Evidence for Recent/Ongoing Activity in Mercury's Praxiteles Basin

Anna Galiano[1], Giovanni Munaretto[2], Deborah L. Domingue[3], Cristian Carli[1], Gianrico Filacchione[1], Valentina Galluzzi[1], Salvatore Buoninfante[1], David Rothery[4], Fabrizio Capaccioni[1], Mario D'Amore[5], Alessandro Maturilli[5], Sebastien Besse[6], Océane Barraud[5], Lauren Jozwiak[7], Antti Penttilä[8], and Oleg Abramov[3]
[1] Institute of Space Astrophysics and Planetology (INAF), Rome, Italy; anna.galiano@inaf.it
[2] Astronomical Observatory of Padova (INAF), Italy
[3] Planetary Science Institute, AZ, USA
[4] School of Physical Sciences, The Open University, UK
[5] Deutsches Zentrum für Luft- und Raumfahrt (DLR), Institute of Planetary Research, Berlin, Germany
[6] European Space Astronomy Centre (ESAC), Spain
[7] Johns Hopkins Applied Physics Laboratory, MD, USA
[8] University of Helsinki, Finland
Received 2025 September 5; revised 2025 December 17; accepted 2025 December 17; published 2026 February 2

Abstract

Mercury's surface, as revealed by the MESSENGER probe, lacks distinctive absorption features in the visible–near-infrared spectral range, except for hollows that display a 630 nm feature ascribed to sulfides. The general absence of spectral features makes inference of its surface mineralogical composition challenging. We inspected the Praxiteles impact basin with newly photometrically corrected MDIS data, removing the influence of topographic shading in the spectra. We detected an 830 nm absorption feature, spectrally compatible with low Fe content minerals. The morphological and spectral correlations suggest that the 830 nm band is linked to geologically recent, or even ongoing, exposure of material, as well as to the early stage of hollow formation. These results provide insight into the subsurface composition of Mercury and imply a crust material locally more oxidized than previously thought.

Unified Astronomy Thesaurus concepts: Mercury (planet) (1024); Infrared spectroscopy (2285); Spectroscopy (1558); Planetary mineralogy (2304)

1. Introduction

The 198 km diameter Praxiteles basin (27.11°N, 60.28°W), located in the Victoria quadrangle (V. Galluzzi et al. 2016), encompasses many spectrally distinct units identified on Mercury's surface, including (1) hollows (R. J. Thomas et al. 2014a; B. De Toffoli et al. 2024), (2) faculae (specifically the Orm faculae; L. Kerber et al. 2011), (3) low-reflectance material (LRM), and (4) low-reflectance, spectrally blue smooth plains (LBP; B. W. Denevi et al. 2009, R. L. Klima et al. 2018). Hollows are shallow, flat-floored depressions with irregular shapes (D. T. Blewett et al. 2011). Some hollows may have bright halos and high-reflectance interiors, interpreted to be the sites of current or recent activity. Hollows exhibiting only bright halos and lacking high-reflectance interiors are mature, whereas hollows with interiors and exteriors spectrally similar to the background are likely inactive (D. T. Blewett et al. 2011, 2013, 2018). The term "facula" (plural "faculae") refers to the spectrally distinct deposits usually associated with explosive volcanic activity on Mercury (S. L. Murchie et al. 2008; R. J. Thomas et al. 2014b). In contrast, the LRM is hypothesized to incorporate higher fractions of carbon from Mercury's original graphite flotation crust (R. L. Klima et al. 2018) and is associated with most hollow-forming areas (R. J. Thomas et al. 2014a, D. T. Blewett et al. 2016). The Praxiteles basin floor is covered by smooth plains, perhaps equivalent to spectrally blue smooth plains (LBP; B. W. Denevi et al. 2009; R. L. Klima et al. 2018) that are younger than the basin-forming event, evidenced by a flooded 25 km impact crater inside the peak ring. We interpret the inside Praxiteles to be the result of effusive volcanism, rather than impact melt or basin ejecta (B. W. Denevi et al. 2013). The presence of several geologic units makes this basin an ideal candidate for spectral investigation to identify potential mineralogical variations.

The mineralogical composition and physical properties of the surface of rocky planets and small bodies can be investigated by the reflectance spectroscopy, which studies the radiation reflected and adsorbed by the terrain when the molecular vibrations cause a change in the dipole moment. As a consequence, the reflectance spectra of minerals in the ultraviolet (UV; 0.1–0.4 μm), visible (VIS; 0.4–0.7 μm), and near-infrared (NIR; 0.7–5.0 μm) ranges manifest absorption bands related to various mechanisms: the electronic transitions within and between atoms, the electronic transition in molecular orbitals (R. G. Burns 1993), and the overtones and combination tones of fundamental vibrational modes of molecules (e.g., G. Herzberg 1945). By studying the absorption bands with specific spectral parameters such as the minimum of the band (i.e., the band center (BC)) and the intensity of the band (i.e., band depth (BD)), information about the mineral species responsible for the feature and their relative abundance can be defined, respectively. The reflectance and spectral slope can be good indicators for the occurrence of dark components and can also provide information about space weathering processes and changes in composition/dimensions of grains.

Both reflectance data acquired by the Mercury Atmospheric and Surface Composition Spectrometer (MASCS; W. E. McClintock & M. R. Lankton 2007) and multispectral images

Original content from this work may be used under the terms of the Creative Commons Attribution 4.0 licence. Any further distribution of this work must maintain attribution to the author(s) and the title of the work, journal citation and DOI.

obtained by the Mercury Dual Imaging System (MDIS; S. E. Hawkins et al. 2007) on board NASA's Mercury, Surface, Space Environment, Geochemistry and Ranging (MESSENGER) spacecraft (S. C. Solomon et al. 2007) show generally featureless spectra across the majority of identified geologic units on Mercury's surface, except for hollows (F. Vilas et al. 2016; A. Lucchetti et al. 2018). Hollows are typically found to be associated with impact structures and sometimes with nearby faculae, such as in Tyagaraja crater (D. T. Blewett et al. 2011; Lucchetti et al. 2021) and Praxiteles basin (D. T. Blewett et al. 2011; V. Galluzzi et al. 2016). MASCS spectra of hollows show a relatively strong curvature shortward of 600 nm (O. Barraud et al. 2020), the highest UV downturn shortward of 400 nm (O. Barraud et al. 2020), and an overall bluer spectral slope in the visible with respect to the Hermean surface (D. T. Blewett et al. 2009). MDIS spectra of hollows located in Dominici, Hopper, Canova, Velazquez, and Tyagaraja craters (F. Vilas et al. 2016, A. Lucchetti et al. 2018, 2021) show a 630 nm absorption feature that can extend from 559 to 828 nm; this feature has been mainly associated with the presence of sulfides (F. Vilas et al. 2016; O. Barraud et al. 2023) and chlorides (Lucchetti et al. 2021; O. Barraud et al. 2023), although additional components could occur, in particular pyroxenes presenting transitional elements such as Cr, Ti, and Ni (A. Lucchetti et al. 2018). Hollows are interpreted to form when volatiles (likely sulfides) are lost after being exposed to the environment owing to sublimation or vaporization caused by micrometeoroid impacts, sputtering by solar ions, or local heating (D. T. Blewett et al. 2013). Two spectra in Dominici's hollows show an 830 nm absorption feature, but no mineralogical association was provided (F. Vilas et al. 2016). A clustering technique applied on MDIS Wide-Angle Camera (WAC) images of these craters shows that clusters of spectra corresponding to hollows are characterized by the 630 nm feature, while clusters surrounding the hollows show spectral properties intermediate between hollows and crater terrain, which have no spectral features (A. Lucchetti et al. 2018, 2021). Concerning Dominici crater, hollows are found both on the crater wall/rim and in its center. The hollows on the crater wall/rim have brighter halos and well-defined edges than hollows in the center of the crater: the stronger 630 nm feature was detected in the crater wall/rim, and a broader feature extending from 559 to 828 nm was found in the center of the crater. The different intensity and shape of the feature were related to a diverse exposure to the Hermean environment: the material on the wall/rim is likely more recently exposed as a consequence of wall slumping, and thus less degraded (F. Vilas et al. 2016). Apart from this 630 nm band, in the MESSENGER data, all other geologic units on Mercury are distinguished merely by differences in reflectance, curvature, or spectral slopes in the enhanced color map (S. L. Murchie et al. 2008; M. S. Robinson et al. 2008; D. T. Blewett et al. 2009; B. W. Denevi et al. 2009). MDIS data of dark and spectrally blue material (such as LRM and some LBP), when normalized for a spectrum of high-reflectance red plain (HRP), show a weak curvature at about 600 nm, related to carbon content (S. L. Murchie et al. 2015; R. L. Klima et al. 2018).

The lack of spectral absorption features is one of the major challenges in our current understanding of the Hermean surface composition and mineralogy.

Thus far, most spectral studies of MDIS data have focused on broader unit characterizations, or on linking the MDIS false-color mosaic to spectral trends, allowing the identification of the major terrains on Mercury (smooth plains, intermediate terrains, and LRM) and the minor units (hollows, faculae, fresh crater ejecta, and red material connected to impact craters; S. L. Murchie et al. 2008; M. S. Robinson et al. 2008; D. T. Blewett et al. 2009; B. W. Denevi et al. 2009). Here we utilize a novel approach focusing on linking small spectral variations with geologic units in order to detect localized mineralogical differences.

Specifically, we performed a detailed investigation of the spectral characteristics of the Praxiteles basin using photometrically corrected MDIS data. By applying a photometric correction to the calibrated data, we removed the influence of shading by the topography or other photometric effects in spectral reflectance (G. Munaretto et al. 2021, 2023), thus minimizing potential artifacts. This correction enhances the likelihood of observing spectral changes associated with real compositional variations. As a result, we detected a spectral feature at 830 nm in localized regions of the Praxiteles basin. We investigated the truthfulness of the feature, and after that, we performed a spectral analysis to detect the mineral responsible for the feature and its distribution.

2. Data and Methods

2.1. Dataset

We investigated the Praxiteles basin using multispectral images (i.e., "cubes") acquired by MDIS-WAC (S. E. Hawkins et al. 2007). Specifically, we examined cubes EW10209546 (365 m pixel^{-1} resolution, 1049 × 1167 pixels) and EW02110680 (874 m pixel^{-1} resolution, 782 × 779 pixels). Each cube contains data with eight filters with bandpasses between 5 and 18 nm (B. W. Denevi et al. 2018): F (centered at 433.2 nm), C (479.9 nm), D (558.9 nm), E (628.8 nm), G (748.7 nm), J (828.4 nm), L (898.8 nm), and I (996.2 nm). At each pixel in each cube, a reflectance spectrum from about 430 to 1000 nm was produced.

The MDIS data were compared with laboratory spectra obtained from the Reflectance Experiment LABoratory (RELAB)[9] resampled to the MDIS-WAC spectral sampling. The laboratory spectra used are epidote (C1RS76, 710–1000 μm size), hematite (CBCC17, 25–75 μm size), rutile (C1PR01, 0–250 μm), forsteritic olivine Fo90 (C1AG08, 0–45 μm), and forsteritic olivine Fo100 (BKR1DD085, 0–45 μm).

We used MDIS Narrow-Angle Camera (NAC) frames with mean pixel resolutions <20 m pixel^{-1} to produce new geological maps of specific areas. The NAC images used were as follows: EN0243912298M, EN0243912305M (Prax-A), EN0243883518M, EN0243912319M, EN0243912326M (Prax-B), EN0243883490M (Prax-C), EN0243797050M (Area1), EN0223615490M, EN0223701874M (Area2), and EN0243854666M (Area3).

2.2. Photometric Correction

To remove the photometric variations due to topography and to normalize all pixels to a standard illumination and viewing geometry (incidence = 30°, emission = 0°, phase = 30°), we applied the well-validated photometric correction using the

[9] https://sites.brown.edu/relab/relab-spectral-database

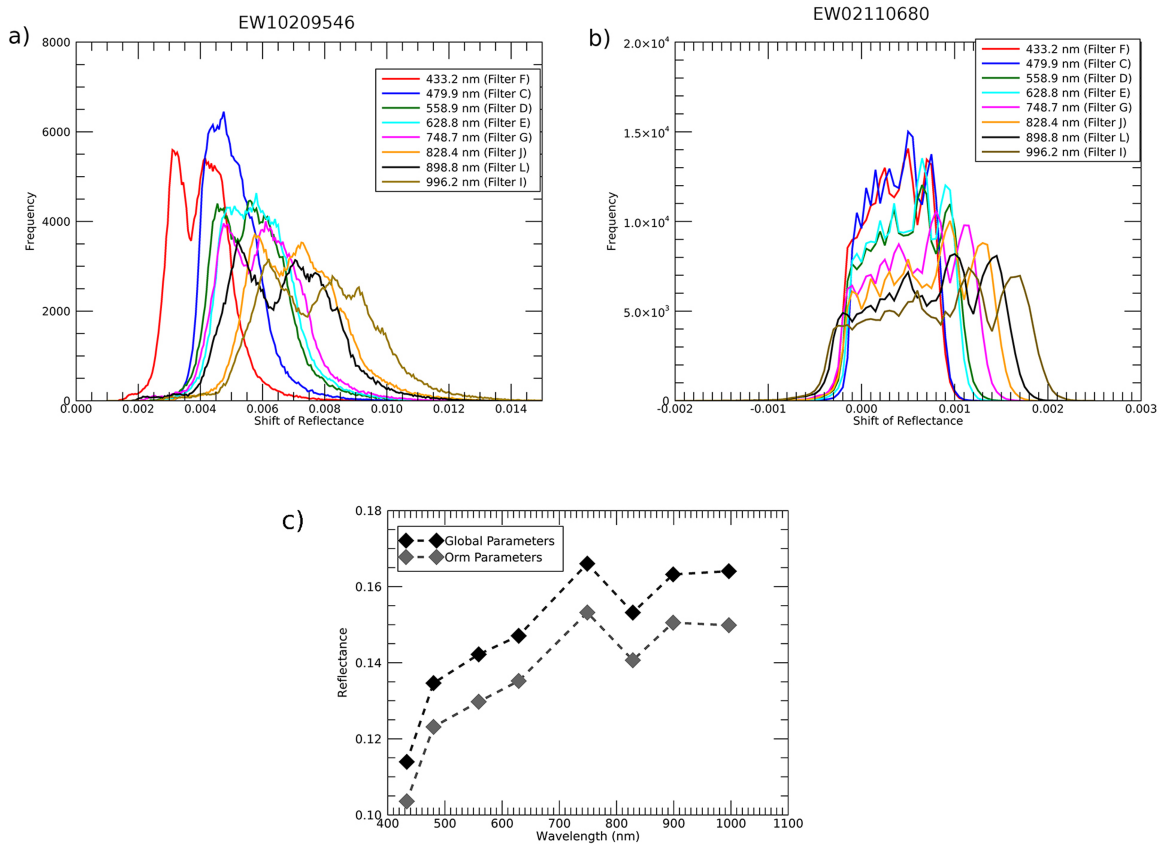


Figure 1. Histogram showing the shift of reflectance between the cube corrected with global parameters and the cube corrected for Orm parameters for each spectral channel for (a) the EW10209546 cube and (b) the EW02110680 cube. The shift is progressively higher toward longer wavelengths for both cubes. (c) A representative MDIS spectrum from the EW10209546 cube (164, 434) showing the 830 nm band corrected for global parameters (gray spectrum) and for Orm parameters (black spectrum); the spectral feature is present in both spectra.

photomet tool in ISIS (see, e.g., A. Lucchetti et al. 2021; M. A. Pajola et al. 2021). This procedure uses the Hapke model based on the global Mercury parameters by D. L. Domingue et al. (2016) and computes the incidence and emission angles at each pixel using the USGS global digital terrain model of Mercury[10] at 665 m pixel^{-1}. In Munaretto et al. (2023), it was noted that for local spectrophotometric analysis this global photometric model of Mercury can be more than 10% off when the specific study sites include surface features significantly different from the average Mercury surface. This is the case in our study region, which has hollows and pyroclastic deposits. To ensure that hollows and pyroclastic deposits present in our study region do not affect our analysis, we applied a local photometric correction (using specific parameters that we refer to as Orm parameters) following the approach and methodology of G. Munaretto et al. (2023; further details are provided in the Appendix). As a result, the two different photometric corrections applied to MDIS data in this work do not produce substantial spectral differences apart from a shift in the overall absolute reflectance level of the entire spectrum (Figure 1). The spectra of the EW10209546 and EW02110680 cubes corrected with global parameters have a higher reflectance level than the spectra of the cubes corrected with the Orm parameters. We performed this analysis for each spectral channel for EW10209546 and EW02110680 cubes (Figures 1(a) and (b)). The shift in reflectance is progressively higher moving toward longer wavelengths for both cubes. However, we found that when the 830 nm absorption feature is present it can be observed in the spectra corrected with both methods (Figure 1(c)), therefore excluding any possibilities for artifacts due to the photometric correction. Thus, the investigation was performed on the cubes corrected for the global Mercury parameters.

[10] https://astrogeology.usgs.gov/search/map/mercury_messenger_global_dem_665m

2.3. Spectral Tools

Several spectral parameters were calculated for the investigation, such as the reflectance value at 750 nm, the spectral slope in the VIS range (VIS slope), the VIS downturn, and the BC and BD of the 630 and 830 nm absorption features.

The VIS slope was estimated in the 480–830 nm range as $\frac{R_{830}-R_{480}}{\lambda_{830}-\lambda_{480}}$, where R_{830} and R_{480} are the reflectance values at 830 and 480 nm, respectively, while λ_{830} and λ_{480} are the corresponding wavelengths expressed in μm. From the literature, the UV downturn in MASCS spectra was calculated by taking into account the reflectance at wavelengths shorter than 350 nm (T. A. Goudge et al. 2014). However, the shortest wavelength of MDIS-WAC spectra is 430 nm; thus, in this work, we extrapolated the VIS downturn using the F filter (430 nm filter) in the MDIS data. In particular, the spectra at 480 and 560 nm were fitted by a linear fit, which was extended down to 430 nm to obtain the extrapolated reflectance for the filter at 430 nm (R_M). Thus, the VIS downturn, in our work, was estimated as the ratio between the modeled reflectance R_M and the measured reflectance at the same filter (R_m). This

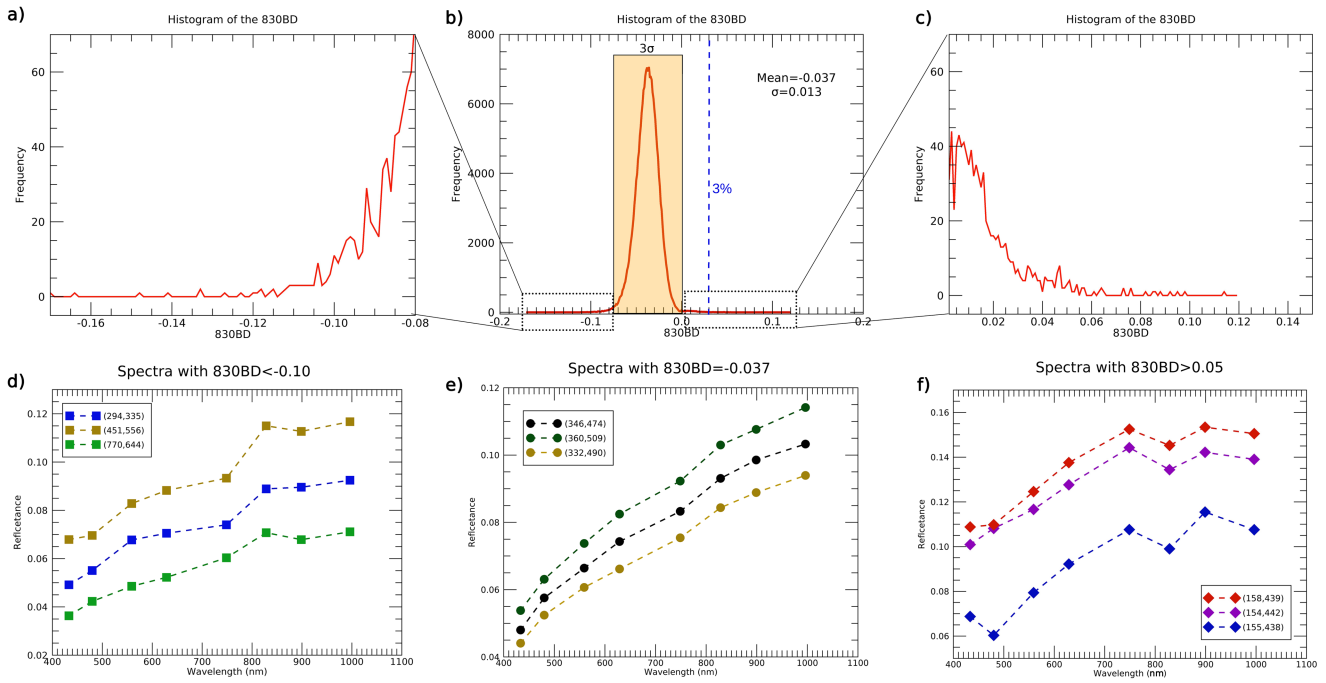


Figure 2. (b) Histogram of the 830BD values, ranging from about −0.17 to about 0.12. The 3σ interval from the mean is represented by the orange box. The BD value of 3% (used as the detection limit) is marked by the dashed blue line. (a) Zoom-in of the left tail and (c) zoom-in of the right tail of the histogram enclosed in black boxes in panel (b). (d, e, f) Representative spectra with 830BD values <-0.10, with 830BD equal to −0.037 (the mean value of the 830BD), and with 830BD greater than 0.05.

parameter is comparable to the UV downturn in MASCS data, since it provides insights into the spectral trend shortward of 430 nm and therefore in the far-UV spectral range.

The 830 nm band was isolated by dividing the MDIS spectra for a modeled spectral continuum fitted by a straight line, whose local maxima were estimated in the 628.8–748.7 nm and 828.4–996.2 nm spectral ranges. Similarly, the isolation of the 630 nm band was performed by removing the fitted spectral continuum, whose endpoints were the local maxima in the 479.9–628.8 nm and 628.8–828.4 nm spectral ranges. Then, on the isolated absorption bands, we estimated the BC and the BD. The BC corresponds to the wavelength where the minimum value of reflectance in the isolated band occurs (R. N. Clark 1999). The BD is the intensity of the spectral feature, estimated as $1 - \frac{R_{\rm BC}}{R_c}$, where $R_{\rm BC}$ is the reflectance at the BC and R_c is the reflectance at the fitted continuum (R. N. Clark & T. L. Roush 1984).

Finally, the Pearson correlation coefficient (PCC) was used to evaluate the possible correlation between spectral parameters (A. L. Edwards 1976). The PCC fits a linear correlation between two variables, X and Y, by considering the covariance of variables ($\mathrm{cov}(X, Y)$) and their standard deviations (σ_X and σ_Y), following the expression $\frac{\mathrm{cov}(X,Y)}{\sigma_X \cdot \sigma_Y}$.

The resulting value ranges from −1 (suggesting a linear anticorrelation) to 1 (suggesting a linear correlation). A PCC near 0 indicates the lack of any statistical correlation between parameters.

2.4. Geological Maps

To produce the novel geological maps of the studied areas, we followed the standard morphological criteria to map linear features, geological contacts, and geological units as described by A. Lucchetti et al. (2018). Linear features were marked to indicate pit borders, crater rims, and crater wall detachments. Crater units were divided into proximal ejecta material, inner crater walls, and smooth or hummocky crater floors. Bright crater wall material not associated with hollows is here interpreted as downslope mass movements such as gully-like features (C. C. Malliband et al. 2018) here referred to as "bright gullies." Additionally, we distinguished between hollow clusters and hollowed terrain in our mapping. Hollow clusters are locations where adjoining hollows have developed to form a contiguous etched terrain (with individual hollows too closely located to be mapped separately); the hollow clusters appear as irregularly shaped depressions, which can be hundreds of meters to a few kilometers wide, whereas hollowed terrains are areas containing small scattered hollows that are not conjoined into a larger formation.

3. Results

3.1. Detection of the 830 nm Absorption Feature

Using the photometrically corrected MDIS data of the EW102096546 cube and EW02110680, we identified several areas within the Praxiteles basin where we detected a reflectance minimum in the 830 nm channel, together with the previously known 630 nm feature.

The histogram of BD values of the 830 nm absorption feature in Praxiteles basin ranges from ∼−17% to ∼12% (Figures 2(a), (b), and (c)). The mean value is negative (−3.7%) since the average spectrum of Mercury lacks the 830 nm band and is red-sloped (spectra of Figure 2(e)). Spectra with a more negative 830BD value, outside the range of 3σ from the mean (where 99.73% of the data are included), are characterized by a peak in the reflectance of the 830 nm filter (green spectrum in Figure 2(d)) or by a minimum in reflectance in the adjacent filters (blue and yellow spectra in

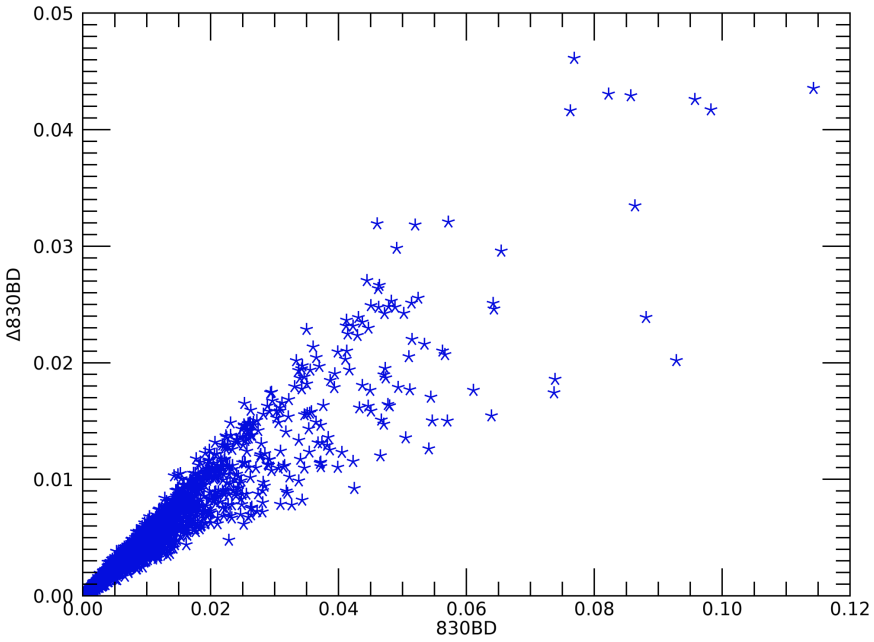


Figure 3. Scatterplot of the 830 nm BD and associated error. For 830 nm bands with an intensity lower than 1% the error is comparable to the BD value. For BD values greater than 3% the errors are progressively smaller than the band's intensity.

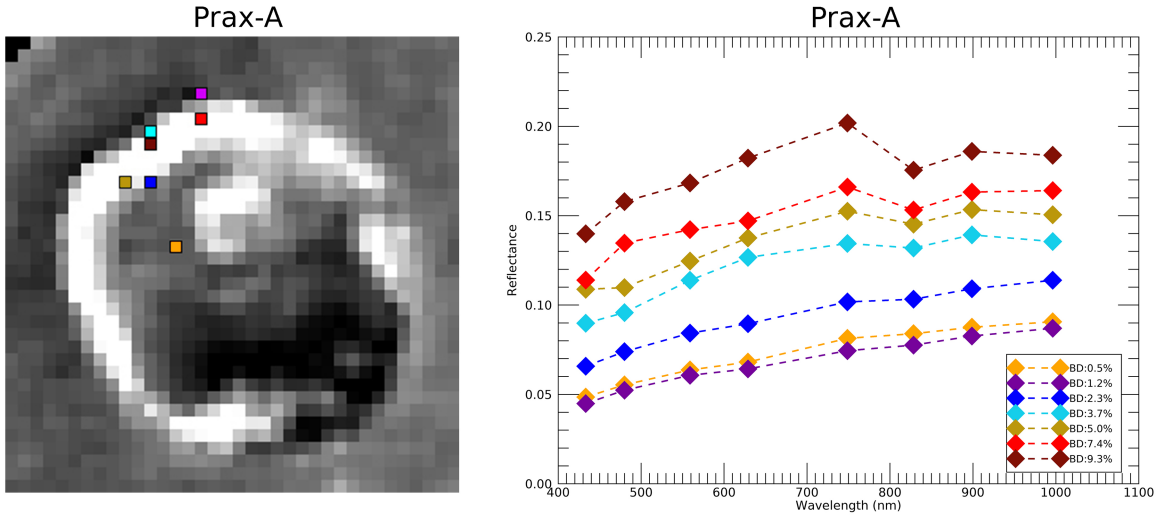


Figure 4. Left: location of the spectra with different intensities of the 830 nm band from within the unnamed crater that we refer to as Prax-A. Right: MDIS single spectra from within Prax-A (whose location is shown in the left panel) with increasing intensity of the 830 nm band. The spectral feature is absent or undetectable for spectra with a BD lower than 3%. The spectra shown in the figure can be found at the following samples and lines in the EW10209546 MDIS cube: 160, 436 (dark-red spectrum); 164, 434 (light-red spectrum); 158, 439 (yellow spectrum); 160, 435 (cyan spectrum); 160, 439 (blue spectrum); 164, 432 (violet spectrum), 162, 444 (orange spectrum).

Figure 2(d)), which could be related to residuals in radiometric uncertainty or to the occurrence of an absorption band in the 560–830 nm range (as already found by A. Lucchetti et al. 2018), respectively. From the literature, radiometric uncertainty in the MDIS data is on average 1.8%–2.3% depending on the filter (B. W. Denevi et al. 2018).

We estimated the error on the 830BD (Δ_{830BD}) by propagating the error on the filters (assuming an average uncertainty in reflectance level of 2%), and we always obtained a lower error than the band's intensity (Figure 3). However, for BD values of about 1% the associated error (whose maximum is 0.7%) has comparable values to the intensity and the band lacks in the spectra, as well as in spectra with a BD value lower than 1% (Figure 4). In addition, a weak and uncertain spectral feature is observed in spectra with values of ∼2% (whose maximum error is about 1%). In these cases, the parameter is likely affected by residual oscillations in the filters (B. W. Denevi et al. 2018), which could produce a nonzero value of the band's intensity. A well-defined band can be observed for BD values $\geqslant$3% (whose maximum error is 1.8%). For BD values larger than 3%, the error is progressively smaller than half of the values of intensity. In addition, the BD value of 3% is far outside the range of 3σ from the mean value in the histogram of BD, suggesting that these spectra are anomalous or worth investigating (Figure 2(f)).

The error on the BD values, the statistical analysis, and the correlation with geospatial location (as shown below) strengthen the hypothesis that the minimum in reflectance

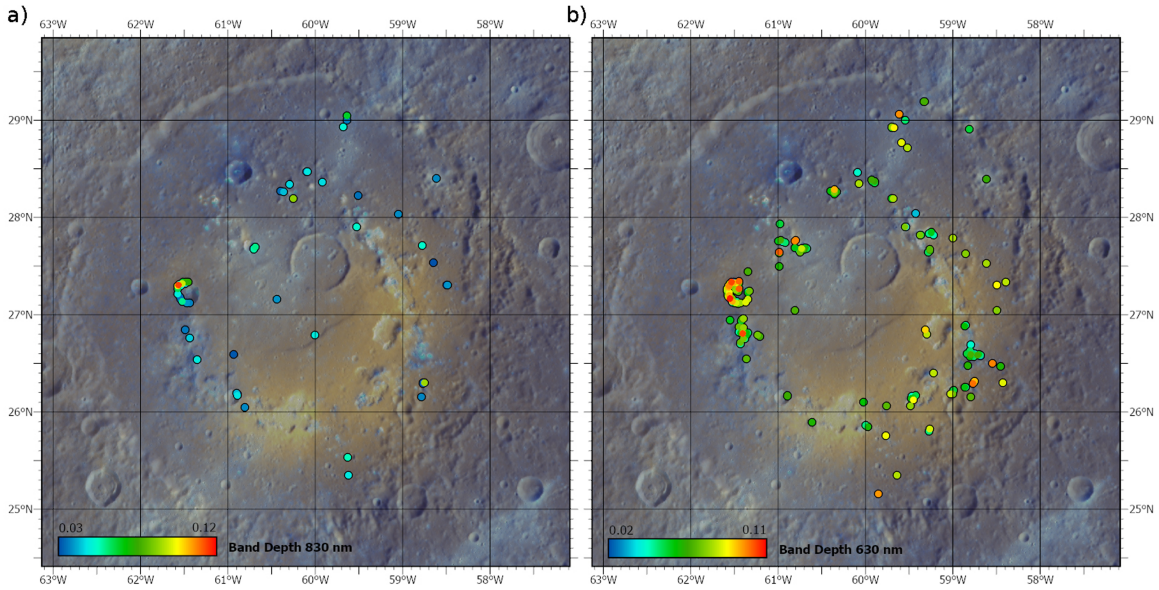


Figure 5. (a) Map of the 830BD for the EW10209546 cube from 3% to 12%. (b) Map of the 630BD for the EW10209546 cube with values from 2% to 11%. Lower values of BDs could be related to radiometric uncertainties.

responsible for the 830 nm absorption feature with an intensity greater than 3% is related not to radiometric oscillations but to the formation of a spectral feature. The value of 3% BD was therefore used as the detection limit of the band. The distribution of the 830 nm band in the Praxiteles basin with BD greater than 3% is shown in Figure 5(a). The basin also hosts areas showing the well-known 630 nm band (Figure 5(b)).

The detection of the 830 nm band occurs in both clustered groups and isolated pixels. To strengthen the veracity of the detection of the spectral feature, we focused the investigation on locations where groups of two or more pixels occur (Table 1) and with a BD value greater than 3%. BD values associated with the 830 nm absorption feature range from approximately 3% to 12%. Detections of this feature are associated with several unnamed craters, referred to here as Prax-A (28.2°N, 60.3°W, ∼10 km diameter), Prax-B (26.1°N, 61.0°W, ∼7 km in diameter), and Prax-C (27.7°N, 60.8°W, ∼5 km in diameter; Figure 6). In addition, three areas that we refer to as Area1 (centered at 28.2°N, 60.3°W, with an area of ∼4 km^2), Area2 (centered at 26.3°N, 58.7°W, ∼0.5 km^2), and Area3 (centered at 28.4°N, 60.1°W, ∼0.3 km^2; Figure 6) also display clusters of pixels with an evident 830 nm band. Prax-A, Prax-B, and Prax-C are interpreted to be relatively young craters, as evidenced by the overall lack of superposed craters within these features. Prax-A, Prax-B, and Area1 are located around the same radius as the Praxiteles peak ring, although the peak ring has a noncontinuous appearance and is largely absent from the portion of the crater floor where these areas are located (Figure 6(b)).

The high-resolution MDIS images acquired with the NAC, combined with the higher-resolution MDIS-WAC cube (EW10209546; Figure 7), reveal that the spectral feature is spatially located on the wall/rim of the Prax-A, Prax-B, and Prax-C craters and in association with hollows exposed on the wall/rim of these craters. The spectral feature identified in Area1, Area2, and Area3 is associated with hollow clusters on the Praxiteles floor.

The high-resolution cube (EW10209546) and the lower-resolution cube (EW02110680) show the 830 nm band in Prax-A, Prax-C, Area1, Area2, and Area3. EW10209546 additionally shows the 830 nm band within Prax-B and in the southeastern wall of Prax-C, which are not observed in the EW02110680 cube (Figure 8), likely limited by the relatively low spatial resolution of the cube. Thus, for our analysis, we decided to present results from the higher spatial resolution EW10209546 cube. The 830 nm absorption feature is not detected in the spectra of other spectral units present in the basin, such as LRM, LBP, and pyroclastic deposits (Figure 9).

The average spectra for Prax-A, Prax-B, and Prax-C are obtained by averaging the individual spectra (normalized at 550 nm) from clusters of 26, 3, and 3 pixels, respectively. The average spectra for Area1, Area2, and Area3 are obtained by averaging the spectra (normalized at 550 nm) of 2, 3, and 2 pixels, respectively (Figure 10). The spectra of Prax-C and Area3 have a similar spectral shape longward of 630 nm and, together with Area2, have an 830 nm absorption feature extending from 750 to 1000 nm. A narrower 830 nm band, ranging from 750 to 900 nm, characterizes the spectra of Prax-A, Prax-B, and Area1.

3.2. Geological Context of the Detected 830 nm Absorption Features

The geological mapping of the study areas produced in this work (Figures 11 and 12) allowed us to better investigate the geological locations of the peculiar spectra showing the 830 nm band.

Within Prax-A (Figure 11, Table 1), most of the pixels showing the 830 nm band are located on bright gullies, fresh wall segments exposed by material slumping, and on the rim crest, upslope of the wall detachments. Two pixels are located coincident with a hollow cluster on the southern wall of the crater. Similarly, Prax-B and Prax-C mapping also revealed hollowed terrain and hollow clusters along portions of the craters' rims and walls (Figure 12, Table 1). At Prax-B, detections of the 830 nm band were made downslope of the hollow cluster along the crater wall (Figures 7(B) and (b),

Table 1
Geological and Spectral Informations about the Studied Areas

Lat (°N)	Lon (°E)	830BD (%)	Location	Geological Setting	Description	630BD (%)
27.32	−61.54	3.2	Prax-A	Bright gullies	Bright gullies and fresh wall detachments	n.d.
27.33	−61.52	3.3	Prax-A	Bright gullies	Bright gullies and fresh wall detachments	9.4
27.18	−61.56	3.4	Prax-A	Shadow	NAC frame is in shadow	n.d.
27.31	−61.53	3.4	Prax-A	Bright gullies	Bright gullies and fresh wall detachments	7.5
27.16	−61.55	3.5	Prax-A	Shadow	NAC frame is in shadow	n.d.
27.12	−61.44	3.6	Prax-A	Wall hollows	Hollow cluster along southern wall	7.9
27.33	−61.53	3.7	Prax-A	Bright gullies	Bright gullies and fresh wall detachments	n.d.
27.12	−61.48	3.9	Prax-A	Wall hollows	Hollow cluster along southern wall	7.2
27.30	−61.54	4.0	Prax-A	Bright gullies	Bright gullies and fresh wall detachments	n.d.
27.32	−61.50	4.1	Prax-A	High wall	Top of crater wall, next to fresh gullies	n.d.
27.31	−61.54	4.7	Prax-A	High wall	Top of crater wall, next to fresh gullies	n.d.
27.22	−61.58	4.8	Prax-A	Rim crest	NAC in shadow, but the point is located on high rim crest	7.1
27.29	−61.55	5.0	Prax-A	High wall	Top of crater wall, next to fresh gullies	n.d.
27.31	−61.56	5.1	Prax-A	Rim crest	On top of rim crest, behind wall detachments	n.d.
27.33	−61.50	5.4	Prax-A	Bright gullies	Bright gullies and fresh wall detachments	n.d.
27.29	−61.57	5.5	Prax-A	Rim crest	On top of rim crest, behind wall detachments	9.1
27.14	−61.53	5.6	Prax-A	Rim crest	NAC in shadow, but the point is located on high rim crest	9.5
27.30	−61.56	5.7	Prax-A	Rim crest	On top of rim crest, behind wall detachments	5.6
27.27	−61.58	6.1	Prax-A	Rim crest	NAC in shadow, but the point is located on high rim crest	n.d.
27.34	−61.47	6.4	Prax-A	Bright gullies	Bright gullies and fresh wall detachments	n.d.
27.34	−61.52	6.4	Prax-A	Rim crest	On top of rim crest, behind wall detachments	2.4
27.34	−61.46	7.4	Prax-A	Bright gullies	Bright gullies and fresh wall detachments	n.d.
27.34	−61.49	7.4	Prax-A	Bright gullies	Bright gullies and fresh wall detachments	n.d.
27.32	−61.53	9.3	Prax-A	Bright gullies	Bright gullies and fresh wall detachments	n.d.
27.29	−61.58	9.8	Prax-A	Rim crest	On top of rim crest, behind wall detachments	n.d.
27.30	−61.57	11.4	Prax-A	Rim crest	On top of rim crest, behind wall detachments	n.d.
26.19	60.91	4.2	Prax-B	Wall hollows	Feature located below incipient hollow cluster forming along a fresh crater wall	n.d.
26.19	60.90	3.1	Prax-B	Wall hollows	Feature located below incipient hollow cluster forming along a fresh crater wall	n.d.
26.17	60.90	4.7	Prax-B	Wall hollows	Feature located below incipient hollow cluster forming along a fresh crater wall	6.5
27.70	60.70	5.7	Prax-C	Wall hollows	Hollow cluster along southeastern wall; high incidence angles	11.0
27.68	60.71	4.5	Prax-C	Wall hollows	Hollow cluster along southeastern wall; high incidence angles	n.d.
27.67	60.71	5.4	Prax-C	Wall hollows	Hollow cluster along southeastern wall; high incidence angles	6.3
28.27	60.40	3.4	Area1	Hollows edge	Feature located at the edge of the largest hollow of a wider hollow cluster	5.8
28.26	60.37	4.2	Area1	Hollows edge	Feature located at the edge of the largest hollow of a wider hollow cluster	n.d.
26.30	58.77	3.2	Area2	Wall hollows	Feature located at the edge or within a hollow cluster that likely follows the edges of a subdued secondary crater	7.8
26.25	58.72	8.8	Area2	Wall hollows	Feature located at the edge or within a hollow cluster that likely follows the edges of a subdued secondary crater	n.d.
26.30	58.76	3.2	Area2	Wall hollows	Feature located at the edge or within a hollow cluster that likely follows the edges of a subdued secondary crater	n.d.
28.47	60.11	3.7	Area3	Isolated hollows	Feature within a small isolated hollow cluster found on Praxiteles floor	n.d.
28.47	60.10	4.7	Area3	Isolated hollows	Feature within a small isolated hollow cluster found on Praxiteles floor	n.d.

Note. The columns describe, for each pixel of the studied areas: the latitude and longitude, the intensity of the 830 nm band (830BD), the corresponding region and geologic setting, descriptive notes, and the intensity of the 630 nm band (630BD) when present (n.d. indicates a 630 nm band not detected).

Figure 12), while detections at Prax-C correspond to the hollow cluster along the southeastern wall of the crater (Figures 7(C) and (c), Figure 12).

Area1, Area2, and Area3 (Figure 12, Table 1) are also hollow-bearing regions. Detections of the 830 nm absorption feature were made at the edge of the largest individual hollow ($\sim$4 km^2) within a larger hollow cluster at Area1, in a hollow cluster at Area2, and in a small isolated hollow cluster at Area3 (Figures 7(D)–(F) and (d)–(f), Figure 12).

3.3. Spectral Characteristics

To further investigate the MDIS spectral properties of the dataset, we related several spectral indices, such as VIS downturn and VIS slope, suitable to qualitatively assess the presence of an oxygen-metal charge transfer (OMCT) band (T. A. Goudge et al. 2014) and color variations (A. Galiano et al. 2023), respectively. The VIS downturn and VIS slope of the spectra showing the 830 nm feature are moderately anticorrelated, with a PCC of −0.65 (Figure 13(a)). This spectral trend is not observed in the regions of LRM, LBP, and pyroclastic deposits (Figure 14), making it peculiar for spectra showing the 830 nm absorption feature. Spectra with lower VIS downturn values and redder spectral slopes are characterized by the presence of only an 830 nm band (Figure 13(b), various red spectra). In comparison, spectra with higher VIS downturn values and flatter slopes (i.e., spectral shapes typical of hollows; D. T. Blewett et al. 2009; O. Barraud et al. 2020) occasionally display both a 630 nm spectral feature and the 830 nm band (Figure 13(b), various black spectra).

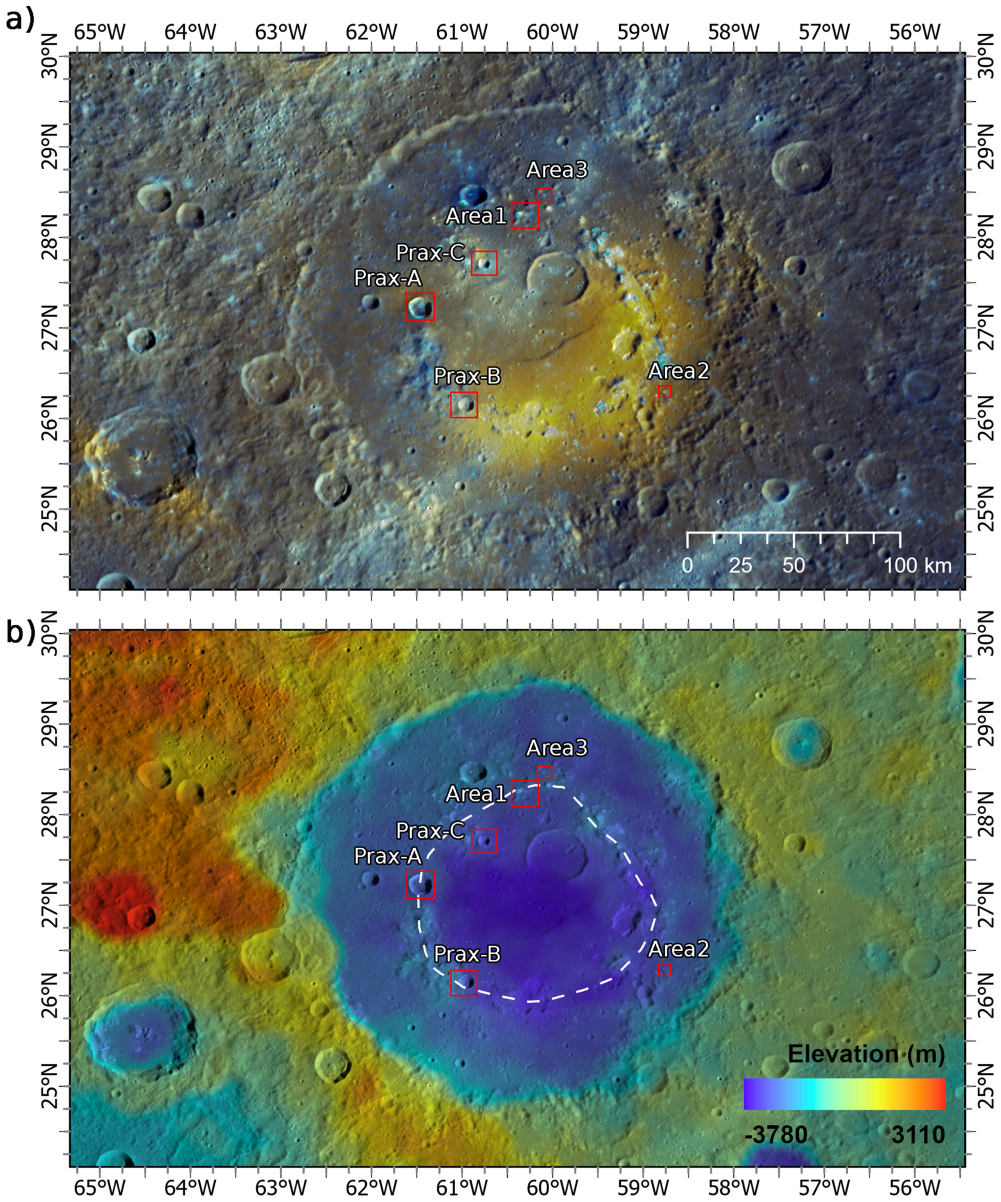


Figure 6. (a) Enhanced color image of Praxiteles basin studied in this work. The grouped areas whose spectra show the 830 nm band are enclosed in red rectangles. (b) Topography map of Praxiteles basin, with the dashed line representing the approximate location of the peak ring, obtained by considering the position of the exposed part of the peak ring.

The 630 nm band (previously detected in hollows' spectra at various other craters; F. Vilas et al. 2016; A. Lucchetti et al. 2018, 2021) was detected in all six study regions in this work (Figure 15). Typically, the 630 and 830 nm bands are not colocated, but there are some locations that have spectra exhibiting both features, including nine pixel spectra within Prax-A, two pixel spectra within Prax-C, and one pixel spectrum within Prax-B, Area1, and Area2. At Area3, no spectra exhibit both features.

The spectra showing both spectral features are found in hollow clusters on the crater walls of Prax-A, Prax-B, Prax-C, and Area2 and on the edge of the hollow in Area1. Additionally, in Prax-A, the spectra with both spectral features are coincident with the locations of bright gullies, fresh wall slumps, and the top of the rim crest, i.e., behind wall detachments (Table 1). There is a weak anticorrelation (PCC of −0.2) between the intensity of the 630 and 830 nm absorption features in spectra where they coexist; a higher intensity of the 630 nm feature is associated with a lower intensity of the 830 nm band (Figure 16). Thus, from this result we can infer that the two features are due to different minerals. There are four statistical outliers (representing 28% of the identified double absorption pixels) to the (albeit weak) trend that do not show a linear relationship between the intensity of the absorption bands: two of these pixels correspond to the rim crest of Prax-A, one is located within a hollow along the wall of Prax-C, and the other one is in the hollow's edge of Area1. This anomalous trend is not linked to any other parameter estimated in the analysis. Thus far, it is not yet clear whether the lack of correlation in band intensities of these four pixels is representative of a specific physical process or just due to a small number of statistics.

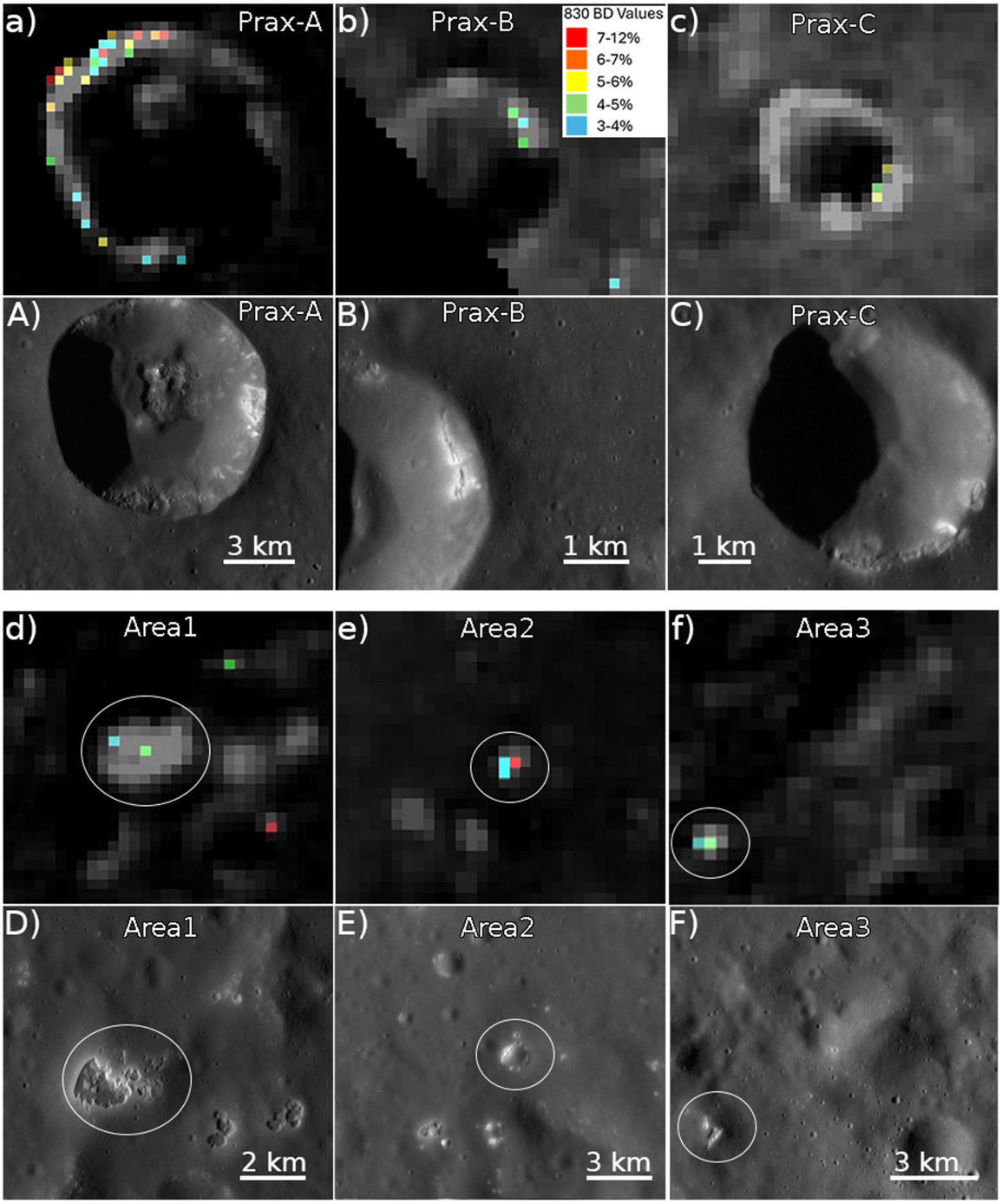


Figure 7. MDIS color image EW10209546 (spatial resolution of 365 m pixel^{-1}) of (a) Prax-A, (b) Prax-B, (c) Prax-C, (d) Area1, (e) Area2, and (f) Area3 and corresponding MDIS-NAC high-resolution images (panels (A)–(F)). Area1, Area2, and Area3 refer to the zone included in the white ellipse in panels (d) and (D), panels (e) and (E), and panels (f) and (F), respectively. The isolated pixels nearby Area1 are excluded. The colored pixels in the images of EW10209546 (panels (a)–(f)) correspond to the locations where the 830 nm feature has been detected and the color code (in panel (b)) provides BD values. The high-resolution MDIS-NAC images, resized and zoomed-in for better clarity, are EN0243912305M (panel (A), ∼18 m pixel^{-1}), EN0243883511M (panel (B), ∼18 m pixel^{-1}), EN0243883490 (panel (C), ∼18 m pixel^{-1}), EN0243797050M (panel (D), ∼17 m pixel^{-1}), EN0223615490M (panel (E), ∼20 m pixel^{-1}), and EN0243854666M (panel (F), ∼17 m pixel^{-1}).

4. Discussion

The 830 nm absorption feature detected in this work differs from most of the spectral features previously discovered in MDIS-WAC spectra of other hollows on Mercury. The spectra of hollows in Dominici crater's south wall/rim mainly show an absorption feature centered at the 630 nm channel (F. Vilas et al. 2016), and in the case of hollows located in Dominici's center and in Canova crater, this feature extends from 560 to 830 nm (A. Lucchetti et al. 2018). An absorption band ranging from 560 to 1000 nm has been found in spectra of hollows in Tyagaraja crater; the feature is centered at the 630 nm channel and is interpreted as either a combination of several absorption features or a single broad absorption band (A. Lucchetti et al. 2021). In contrast to these previous features, the spectral feature observed here in Praxiteles basin manifests a

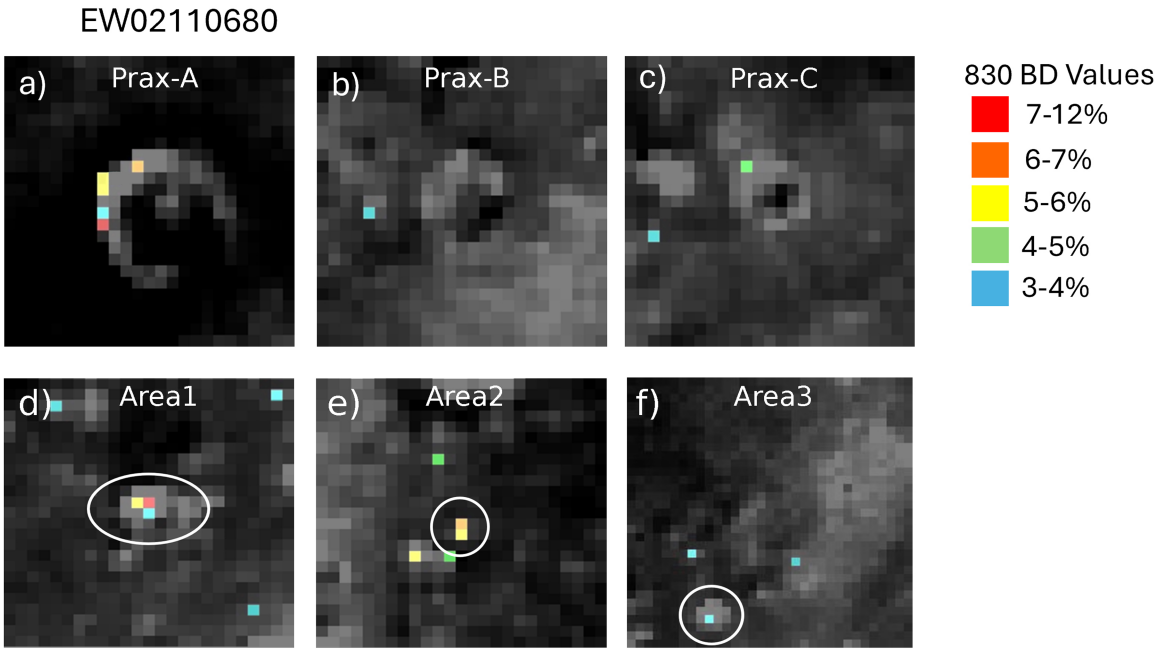


Figure 8. MDIS color image EW02110680 showing the geospatial location of the 830 nm band in (a) Prax-A, (b) Prax-B, (c) Prax-C, (d) Area1, (e) Area2, and (f) Area3. The colored pixels correspond to the spectra with the 830 nm band, and the color code indicates BD (830BD) values (%).

distinctive absorption band with the minimum at the 830 nm channel, and it can extend from ~750 to 1000 nm. Two spectra with a similar feature can be seen in Dominici wall/rim hollows (blue and yellow spectra in Figure 2 of F. Vilas et al. 2016), although no mineralogical attribution was proposed. The 830 nm band suggests the presence of a different composition than that already proposed to explain the 630 nm feature in other hollows.

To identify potential candidate minerals, we compared the MDIS data showing the 830 nm band with laboratory spectra deconvolved to the MDIS spectral sampling. In particular, the laboratory spectra, made of hundreds of channels in the 430–1000 nm range, are reduced to eight channels at the same wavelengths of MDIS-WAC spectra. The reflectance level for each channel was obtained by averaging the reflectance values in the range of wavelengths corresponding to the bandpass filter for each band (18, 8.9, 4.6, 4.4, 4.5, 4.1, 4.3, and 12.0 nm, respectively, taken from S. E. Hawkins et al. 2007) and centered at the wavelength with the same value of spectral channel.

In general, various transition metal ions in a crystalline structure can give rise to an absorption band in the 750–1000 nm spectral range, due to crystal field transitions (R. G. Burns 1993). We identified some laboratory spectra that show a spectral feature in a similar position to that found in this work, which are the hematite (Fe_2O_3) and rutile (TiO_2) oxides, the epidote (a sorosilicate mineral rich in Ca, Al, and Fe), and two samples of olivine with low Fe content (Fo100 and Fo90; Figure 17). In the case of hematite and rutile, the absorption band is ascribed to the occurrence of Fe^+ and Ti^+ in an octahedral coordination site (R. G. Burns 1993), respectively, while the feature in the spectrum of epidote is due to an Fe^+ in the octahedral distorted M3 site (R. G. Burns 1993). The 830 nm feature, which can be observed in spectra of olivine with low Fe content (Figure 17), is related to Fe^{2+} ions in the M1 octahedral coordination site (J. M. Sunshine & C. M. Pieters 1998).

The band position is a good indicator to detect the mineral species responsible for the absorption; thus, we can declare that the 830 nm band here detected is related to the occurrence of metal ions. Spectra of the MDIS cube and laboratory spectra used for the comparison show some differences in reflectance level, spectral slope, intensity, and width of the feature in the 750–1000 nm range (Figure 17). These discrepancies are probably related to the purity of the pixel in the MDIS cube, where the spectra of each single pixel are the contribution of different unidentified minerals composing Mercury's surface.

The spectral analysis highlighted a low VIS downturn parameter in the spectra with a stronger 830 nm band, which could indicate a deepening of the OMCT absorptions, occurring between oxygen and transition metals such as Fe^+ and Ti^+ (R. G. Burns 1993, E. A. Cloutis et al. 2008). Decreasing Fe content in silicate minerals and glasses causes a weakening in the OMCT band, a shift of the shoulder toward shorter wavelengths, and an increase in reflectance. The overall effect of these changes is that lower amounts of Fe will result in higher reflectance and a steeper UV slope (e.g., B. Rava & B. Hapke 1987; E. A. Cloutis et al. 2008; A. S. Greenspon et al. 2012). Thus, a higher amount of Fe could produce a more gentle UV slope and a lower UV downturn, and consequently a lower VIS downturn. The OMCT bands are sensitive to very small amounts (<0.001 wt-%) of Fe^{3+} and Fe^{2+} (E. A. Cloutis et al. 2008). Given the lower mean abundance of Ti (<1%) than that of Fe (1–4 wt%) on Mercury's surface detected by MESSENGER's X-Ray Spectrometer (C. E. Schlemm et al. 2007), Fe is a more plausible source than Ti for the OMCT band (N. R. Izenberg et al. 2014).

In the specific case of olivines, these minerals are characterized by a wide 1.0 μm band, which is the contribution of three absorptions: the central absorption (at about 1000 nm) is due to the crystal field transition of Fe^{2+} in the M2 site, while the absorptions at shorter (about 900 nm) and longer wavelengths (about 1200 nm) are related to the crystal field

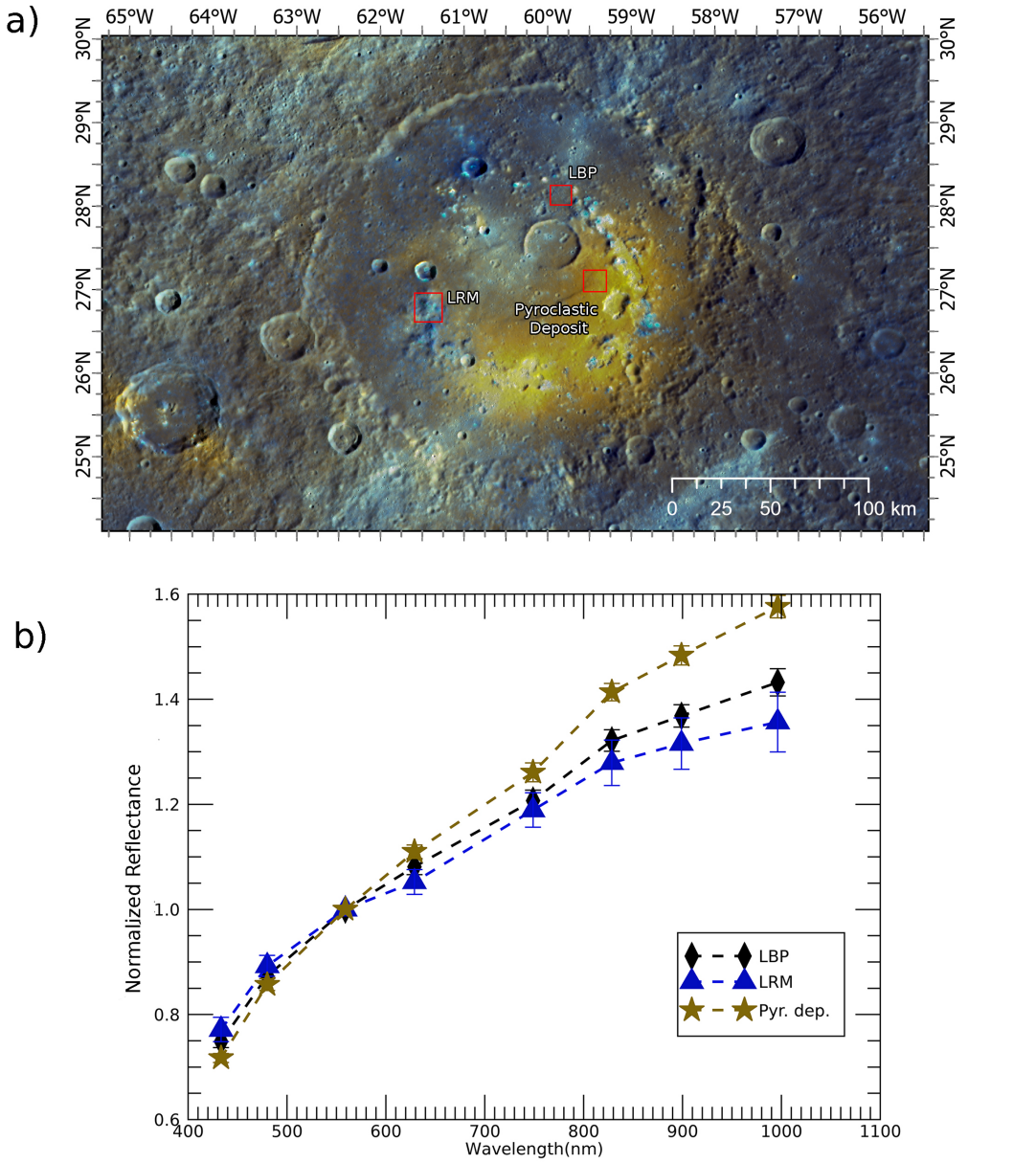


Figure 9. (a) Enhanced color image of Praxiteles basin. The areas enclosed in red rectangles are representative spectral units of LRM, LBP, and pyroclastic deposits. (b) Average spectra, obtained by averaging individual spectra (normalized at 550 nm), of the LBP, LRM, and pyroclastic deposit regions highlighted in panel (a), where no 830 nm feature is observed.

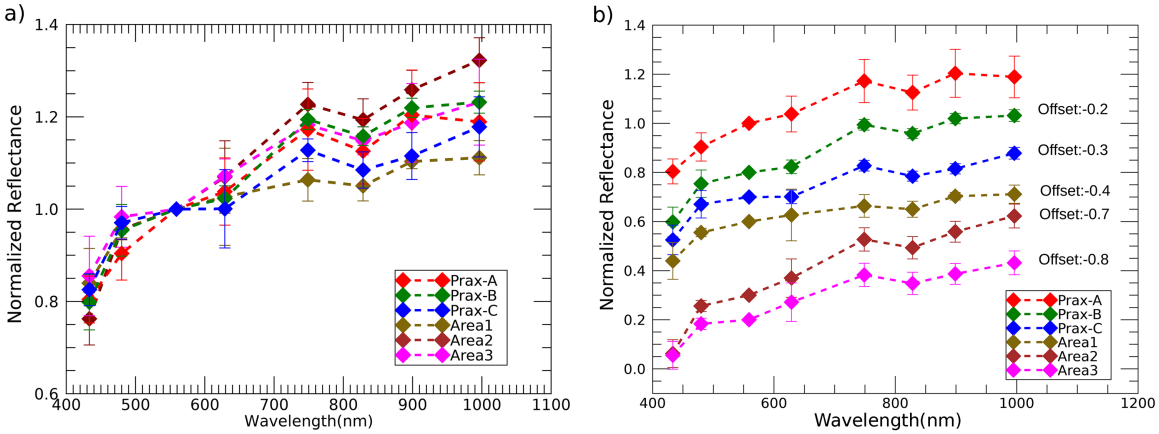


Figure 10. (a) Average normalized spectra of the studied areas and corresponding standard deviation. (b) Same spectra as in panel (a), but where an offset at the reflectance was applied for clarity. The 830 nm band extends from 750 to ∼1000 nm.

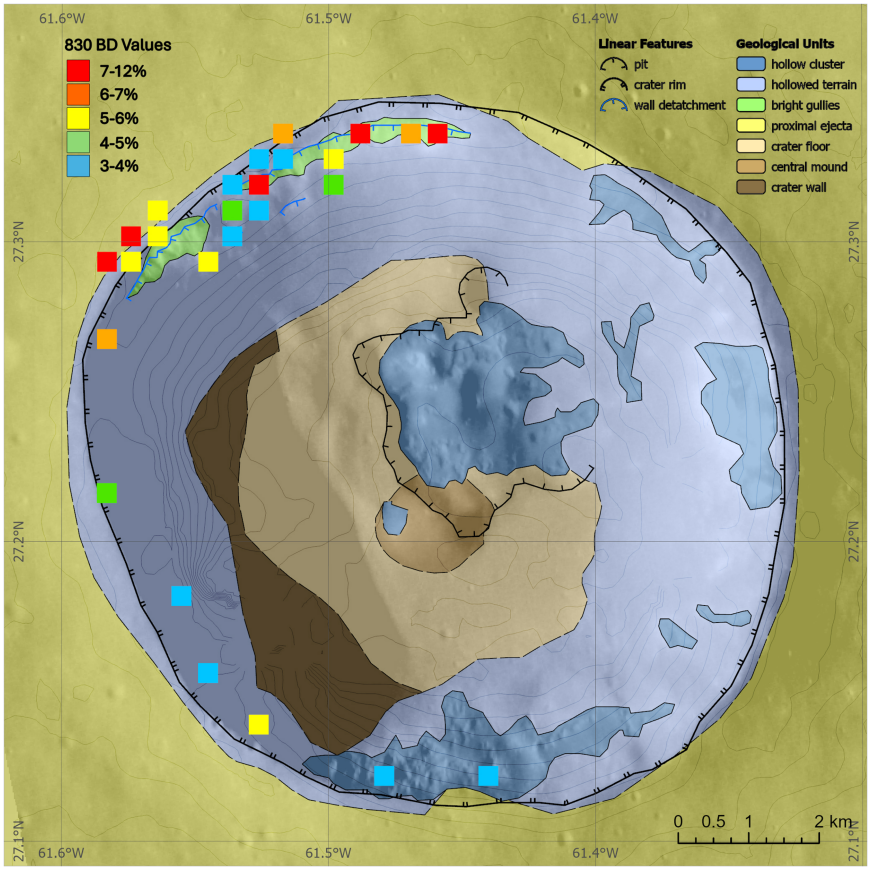


Figure 11. High-resolution (lower than 20 m pixel^{-1}) geological map of Prax-A, where the pixels showing the 830 nm BD above the 3% detection limit are superposed on it.

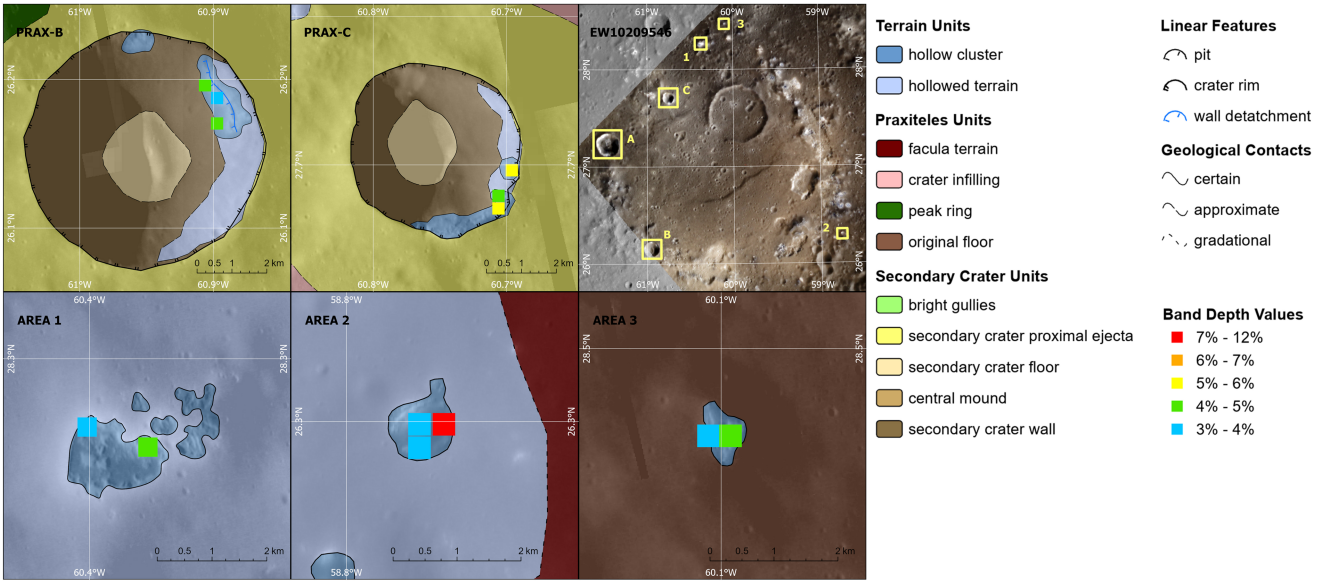


Figure 12. High-resolution (lower than 20 m pixel^{-1}) geological map of Prax-B, Prax-C, Area1, Area2, and Area3. The location of pixels displaying spectra with an 830 nm BD greater than 3% is superposed on the geological map of the study areas.

transition of Fe^{2+} in the M1 site (J. M. Sunshine & C. M. Pieters 1998). It has been studied that the band position of these absorptions moves toward longer wavelengths at increasing Fe content, i.e., from forsteritic olivine (Mg-rich olivine) to fayalitic olivine (Fe-rich olivine) for the substitution of Mg^{2+} with slightly larger Fe^{2+} ions (R. G. Burns 1993; J. M. Sunshine & C. M. Pieters 1998). In olivine with lower Fe content, the band at shorter wavelengths can reach about 800 nm (J. M. Sunshine & C. M. Pieters 1998), and in fact, the laboratory spectra of forsteritic olivines shown in Figure 17 have a minimum at 830 nm. The 830 nm band is also present in the synthetic spectrum of Fo100 produced by

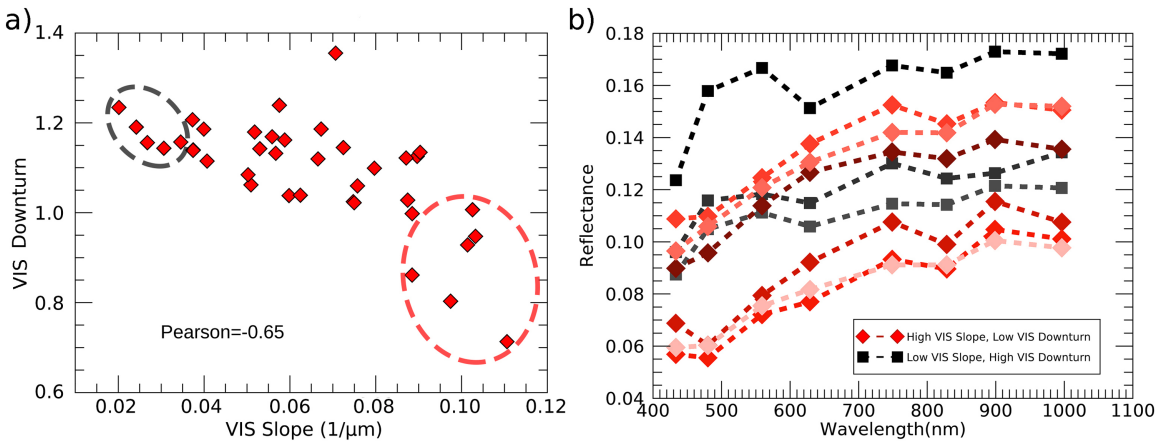


Figure 13. (a) Scatterplot of the VIS spectral slope vs. VIS downturn of the spectra where the 830 nm absorption feature was detected. The moderate anticorrelation (PCC = −0.65) is linked to the co-occurrence of the 630 and 830 nm bands (as observed in panel (b)). (b) Red spectra are those with the reddest VIS spectral slope and lowest VIS downturn (red dashed ellipse in panel (a)), showing only the band at 830 nm. Dark spectra manifest, in addition to a flatter VIS slope and high VIS downturn, 830 and 630 nm features (dashed black ellipse in panel (a)).

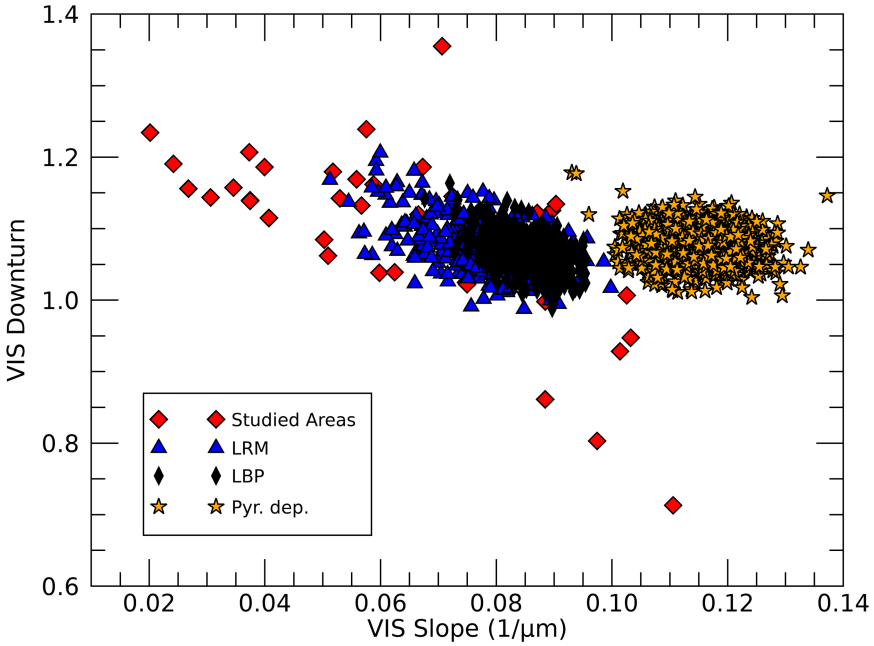


Figure 14. Scatterplot of the VIS spectral slope vs. VIS downturn of the studied spectra where the 830 nm absorption feature was detected (red diamonds; marked in Figure 6) and of representative regions of LRM (blue triangles), LBP (black thin diamonds), and pyroclastic deposits (orange stars) within Praxiteles basin marked in Figure 9(a). The anticorrelation trend observed in the spectra showing the 830 nm band does not occur in LRM, LBP, and pyroclastic deposits regions.

M. D. Dyar et al. (2009; violet spectrum in Figure 17): the occurrence of this band in the spectrum of a Mg-rich olivine could suggest some residuals of Fe in the sample.

Thus, it may be plausible that the MDIS band at 830 nm could be related to low Fe content in minerals and/or in mafic minerals. This interpretation is supported by the location of the basin in a region with a relatively high Fe/Si ratio (L. Nittler et al. 2020), which is also coincident with the high-Mg region (L. Nittler et al. 2020). As a consequence, the localized areas of Praxiteles basin showing the 830 nm band contain, although in low amounts, more Fe than the other regions on Mercury. Furthermore, the high-Mg region is characterized by an enhancement of both S and Ca (L. Nittler et al. 2020), and sulfide minerals are hypothesized to be the main source of the 630 nm feature detected in several hollow regions on Mercury (F. Vilas et al. 2016; A. Lucchetti et al. 2018), including Praxiteles basin (Figures 5(b), 15).

The pixel cluster displaying the 830 nm band within Prax-A is located mainly at the edges of the mapped bright gullies along the wall (Figure 11). From our morphological analysis, it seems that hollow clusters along the wall originally developed from wall detachments and are likely initiated by mass-wasting processes given the steepness of the walls. The fact that 73% of the spectra with the 830 nm absorption feature in Prax-A are located in correspondence with the bright gullies and not within the hollows indicates that this band is linked to the exposure of material by ongoing mass-wasting processes (e.g., C. Aubry et al. 2021) that will potentially develop hollows along the same detachment. Prax-B and Prax-C show the absorption feature in hollow clusters likely exposed by mass-

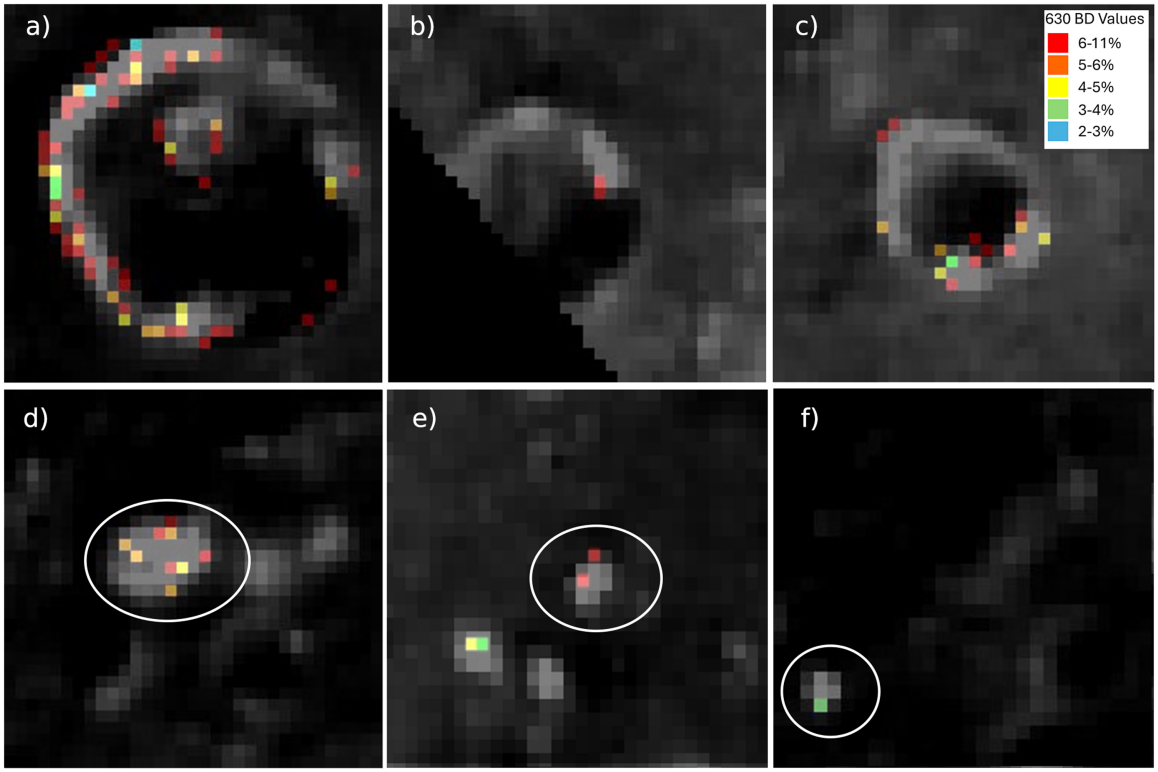


Figure 15. Geospatial location in the MDIS color image EW10209546 of the 630 nm feature in (a) Prax-A, (b) Prax-B, (c) Prax-C, (d) Area1, (e) Area2, and (f) Area3. The colored pixels correspond to the spectra with the 630 nm band, and the color code indicates BD (630BD) values (%).

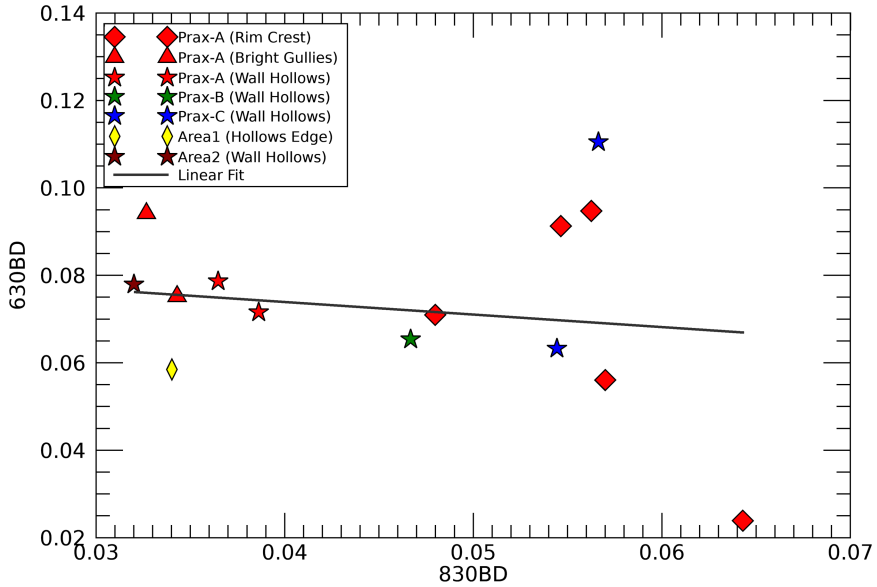


Figure 16. Scatterplot of the 630 nm BD vs. the 830 nm BD. A weak anticorrelation (Pearson coefficient of −0.2) is found between the spectral features, when fitted to a linear relationship represented by the black line.

wasting processes, whereas Area1 shows the absorption band at the edge of hollow clusters. Area2 and Area3 are too small to assess the morphological location of the absorption band with the available MDIS-NAC images.

Hence, from our analysis, the 830 nm absorption is observed in material recently exposed by mass wasting or in the early stage of hollow formation, suggesting that this feature is related to more recent/ongoing processes. Thus, the low Fe mineral responsible for this spectral feature dominates the relatively young/fresh material in the Praxiteles basin.

This conclusion is supported by the observation of the 830 nm absorption feature near regions that are seemingly early in the process of forming hollow clusters, but not in the spatially extensive hollow formation regions, or regions of fully developed (haloless) hollows. In fact, haloless hollows located on the floor of Prax-A (Figure 7(A), (a), Figure 11) do not have the 830 nm absorption; these hollows are suggested to be less active or older than the hollows on crater walls that do host bright halos (A. N. Deutsch et al. 2025). A possible explanation for the lack of the 830 nm band in relatively older

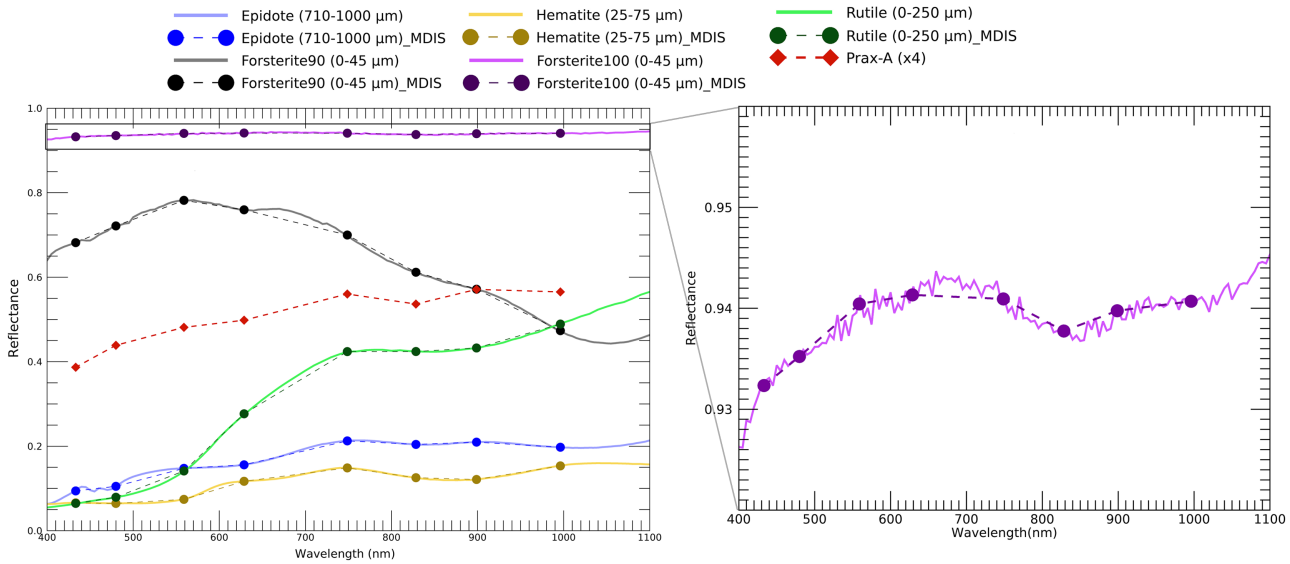


Figure 17. Comparison between the laboratory spectra of epidote, hematite, rutile, and two forsteritic olivines and the average MDIS spectrum of the Prax-A pixels that show the 830 nm band (left panel). The laboratory spectra are shown both with the original spectral sampling (solid lines) and weighted with the channel response of MDIS (dashed lines) to ensure commensurability with the measured data. In the right panel, the reflectance value is stretched in a spectral range useful to visualize the 830 nm band in the laboratory spectrum of Fo100 olivine.

hollows could be related to the exposure of Fe material to the harsh Hermean environment. It is well-known that space weathering processes such as micrometeoritic impacts and solar wind irradiation are responsible for reddening and darkening of the spectra in the VIS–NIR range, as well as the removal of spectral features (B. Hapke 2001; R. Brunetto & G. Strazzulla 2005; D. T. Blewett et al. 2009): space weathering could act on hollows over time and remove the 830 nm band. In fact, the 630 nm band is also usually observed in relatively fresher hollows, where the volatile component responsible for the band (likely sulfides) is less affected by space weathering (F. Vilas et al. 2016). The detection of the 630 nm feature together with the 830 nm band in the study areas supports the thesis of the relatively recent exposition of this material.

The anticorrelations between the 830 and 630 nm bands and between VIS slope and VIS downturn are, together with morphological evidence, hints of local spatial correlations between the two components and disregard a genetic link. As already stated, the spectral reddening can be an effect of space weathering processes, and the hollows, which are spectrally brighter and with a less red slope, are among the youngest and least altered terrains on the planets (M. S. Robinson et al. 2008; D. L. Domingue et al. 2014). Since the investigated areas showing the 830 nm band involve hollows in the early stage of their formation, their redder spectra can be ascribed not to maturity effects but rather to compositional/mineralogical differences. Based on S. Z. Weider et al. (2014), iron on Mercury's surface is highly reduced and partitioned into metal and/or sulfide phases in the regolith. If the iron were embedded within sulfides, we would expect a correlation between the 830 and 630 nm absorption features and the occurrence of the 830 nm band in all active hollow clusters, which is not the case. Perhaps low iron content is present in the crystalline structure of Fe-bearing minerals in association with (but not incorporated into) the volatile component. The two components could have a subsurface origin at a depth of a few kilometers (based on the peak ring basin formation from H. J. Melosh 1989 and D. M. Baker & J. W. Head 2015); the impact that generated the basin likely excavated these materials and transported them to the near surface, which have later been exposed by impacts and/or mass-wasting movements. The occurrence of Fe-bearing minerals on the surface could also explain the existence of several pyroclastic vents found in the basin (V. Galluzzi et al. 2016) and produced by explosive eruptions. The oxidation of volatile elements in Mercury's melt through the assimilation of Fe^{2+} or Ti^{4+} species would cause a major magma degassing (M. Y. Zolotov 2011).

The discovery of sulfides on Mercury's surface with MESSENGER data suggested that the crust's interior could host a higher abundance of volatile elements (D. T. Blewett et al. 2011) than expected based on reduced conditions in which Mercury likely formed (M. Y. Zolotov 2011). The putative detection of low Fe-bearing minerals, together with volatile components in the upper layer of Mercury's crust, strengthens the hypothesis that the crust is locally less reduced.

Due to the low spectral resolution of the MDIS-WAC data (which could hide narrower spectral features) and the restricted wavelength range of the data, it was not possible to be more precise about the low Fe-bearing mineral producing the 830 nm absorption feature. A clearer picture is likely to be obtained by the upcoming BepiColombo mission, thanks to the high spectral and spatial resolution data that will be acquired by the Spectrometer and Imaging for MPO (Mercury Planetary Orbiter) BepiColombo Integrated Observatory SYStem (SIMBIO-SYS) instrument suite (G. Cremonese et al. 2020) and the Mercury Radiometer and Thermal Infrared Spectrometer (MERTIS) TIR imaging spectrometer (H. Hiesinger et al. 2020) aboard the spacecraft.

5. Conclusions

The Praxiteles basin was investigated by using photometrically corrected MDIS data to remove the effects due to topography in reflectance spectra. We detected a spectral feature with a minimum corresponding to the 830 nm channel

in three craters and three areas hosting hollows within the basin. Geological inspection allowed us to associate the band with relatively young/fresh material, such as bright gullies recently exposed by mass-wasting processes or hollows at the early stage of their formation. This evidence suggests that the 830 nm spectral feature is related to more recent or even ongoing processes.

The spectral investigation allowed us to ascribe the 830 nm band to the crystal field transition of Fe^{+} ions in an octahedral coordination site (R. G. Burns 1993) and, in particular, to minerals with low Fe content. This hypothesis is supported by the location of the basin in a region with a relatively high Fe/Si ratio (L. Nittler et al. 2020), highlighting that the Fe in Praxiteles basin is (although in low amounts) more abundant than in the other Hermean regions.

The well-known 630 nm band, ascribed to sulfides, was also detected in the Praxitels basin. The analysis of spectral parameters such as the depth of the 630 and 830 nm bands, the VIS downturn, and the VIS slope suggests that the two components (Fe-bearing minerals and sulfides) could lie in the subsurface of Mercury at a depth of a few kilometers, transported to the surface as a consequence of the impact that generated the basin and recently exposed by secondary impacts and/or mass-wasting movements.

Previous works based on the analysis of remote-sensing spectral data did not observe the 1 μm band ascribed to Fe^{2+} (D. T. Blewett et al. 1997; J. Warell & D. T. Blewett 2004; D. T. Blewett et al. 2009; W. E. McClintock et al. 2008). Ground-based observations of Mercury detected a band centered at 1.1 μm at $-170°$E longitude in both north and south midlatitudes, ascribed to FeO in Ca-rich clinopyroxene (J. Warell et al. 2006). However, the band lacks at $-260°$E longitude, suggesting a variability of the iron in silicates on regional scales on Mercury's surface (J. Warell et al. 2006). The 830 nm band found in this work represents the first spectral detection of Fe on Mercury by using remote-sensing data, and its occurrence on localized and relatively fresh areas strengthens the hypothesis that the crust is locally less reduced.

Acknowledgments

This research was supported by the International Space Science Institute (ISSI) in Bern, through ISSI International Team project No. 552 (Wide-ranging characterization of explosive volcanism on Mercury: origin, properties, and modifications of pyroclastic deposits).

D.L.D., L.J., and O.A. were also supported by NASA grant 80NSSC21K0165 "Pyroclastic Eruption Conditions on the Moon and Mercury."

O.B. is supported by the Alexander Von Humboldt Foundation Research Fellowship program.

V.G. and S.B. acknowledge funding from the Italian Space Agency (ASI) under ASI-INAF agreements 2017-47-H.0 and 2024-18-HH.0. G.M. and A.G. acknowledge funding from the Italian Space Agency (ASI) under ASI-INAF agreement 2017-47-H.0.

We are grateful to the two anonymous reviewers and the editor for their insightful suggestions and constructive comments, which significantly enhanced the quality of this paper.

Data Availability

MESSENGER MDIS data obtained from the NASA Planetary Data System (Cartography and Imaging Sciences Node PDS 2022, doi:10.17189/BDXT-4C65). The photometrically corrected cubes used in this work can be available after specific request to the author.

Code Availability

The data analysis discussed in this paper has been made by means of proprietary software developed in IDL-ENVI language by A.G.

Competing Interests

The authors declare that they have no conflicts of interest or competing interests in undertaking this work.

Appendix

A.1. Photometric Modeling Details

We followed the approach described in G. Munaretto et al. (2023) and mosaicked the C. I. Fassett (2016) digital elevation models (DEMs) of Orm faculae and the USGS global DEM of Mercury and resampled the result at 665 m pixel^{-1} spatial resolution. The C. I. Fassett (2016) DEMs were shifted vertically to match the average elevation of the USGS DEM. The mosaic is shown in Figure 18(a). A 665 m pixel^{-1} grid was defined, with each grid point matching with a pixel within the DEM. All rasters were coregistered and resampled to this resolution, and the local incidence, emission, phase, and azimuth angles were computed with the ISIS phocube routine. For each grid point, the flux and photometric angles were collected for each observation, and these data were fitted with a basic Hapke model. Wavelength-dependent Hapke parameters for the Orm facula pyroclastic deposits were estimated by averaging three regions of interest (ROIs) showing uniform, flat terrain within the faculae (Figure 19). Although the full analysis of the photometric properties of the Orm faculae as implied by the photometric modeling results is being prepared in a future work, we report the Hapke parameters used for the photometric correction in Table 2. These Hapke parameter values were used to perform the photometric normalization of the spectral cube (i.e., ratio of the I/F predicted by the Hapke model at the photometric angles of the observation and multiplication to the I/F predicted by the Hapke model at the standard angles, incidence $= 30°$, emission $= 0°$, phase $= 30°$).

However, coming from a stereo-photogrammetric pipeline, the C. I. Fassett (2016) DEMs have intrinsic noise that could propagate to the photometrically corrected cubes and be significant for relatively small areas like the one we are interested in for the absorption feature analysis. Therefore, we kept the original USGS DEM (Figure 18(b)) for the spectrophotometric normalization. In this way, the parameters for the photometric correction are enhanced, but we do not introduce significant noise in the spectra. In other words, the photometric parameter values were derived using the combined C. I. Fassett (2016) and USGS DEMs for providing the photometric angles (incidence, emission, phase, and azimuth). However, the application of the photometric correction was performed using the photometric angles derived solely from the USGS DEM to provide consistency across the entire study area.

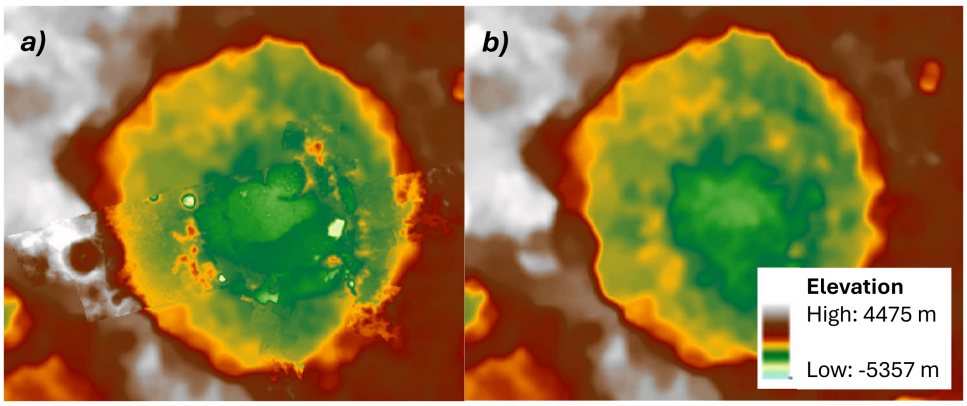


Figure 18. (a) Mosaic of C. I. Fassett (2016) Praxiteles DEMs and the USGS global DEM. (b) USGS global DEM. Both DEMs are resampled at the same resolution (665 m pixel^{-1}) and are displayed with the same color bar and linear stretch.

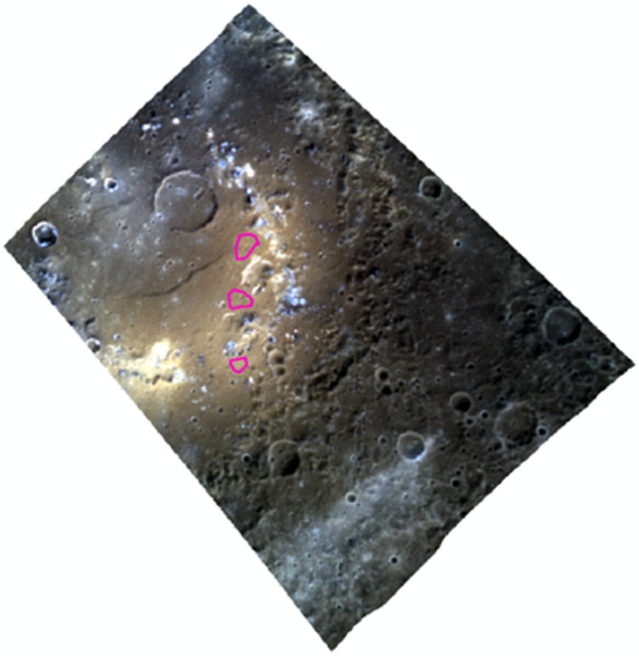


Figure 19. RGB color composite of bands *I* (Red), *G* (Green), and *F* (Blue) of MDIS spectral cube EW10209546 showing the location of the three ROIs used for deriving the Hapke parameters for pyroclastic deposits.

Table 2
Average Hapke Parameters from the Three ROIs in Figure 19

Filter	λ	w	b	c	θ
F	433.20	0.1966	0.1357	0.7096	21.9560
C	479.90	0.2304	0.1375	0.7159	20.5020
D	558.90	0.2709	0.1243	0.7254	20.5177
E	628.80	0.2980	0.1232	0.7270	19.4303
G	748.70	0.3385	0.1038	0.7986	20.3064
L	828.40	0.3769	0.1099	0.7423	19.2851
J	898.80	0.3936	0.1056	0.7480	20.8316
I	996.20	0.4126	0.1005	0.7463	20.8469

Note. λ represents the center wavelength of the filter, w is the single scattering albedo, b is the anisotropy parameter in the single particle scattering function, c is the forward versus backward scattering parameter in the single particle scattering function, and θ is the topographic roughness.

ORCID iDs

Anna Galiano https://orcid.org/0000-0001-8740-0653
Deborah L. Domingue https://orcid.org/0000-0002-7594-4634
Gianrico Filacchione https://orcid.org/0000-0001-9567-0055
Lauren Jozwiak https://orcid.org/0000-0001-7946-5633
Antti Penttilä https://orcid.org/0000-0001-7403-1721

References

Aubry, C., Conway, S. J., Malliband, C., Galluzzi, V., & Giacomini, L. 2021, A Survey of Landforms Indicating Slope Processes in the Mid-latitudes of Mercury, EPSC, 15, 490
Baker, D. M., & Head, J. W. 2015, Constraints on the Depths of Origin of Peak Rings on the Moon from Moon Mineralogy Mapper Data, Icar, 258, 164
Barraud, O., Doressoundiram, A., Besse, S., & Sunshine, J. M. 2020, Near-Ultraviolet to Near-Infrared Spectral Properties of Hollows on Mercury: Implications for Origin and Formation Process, JGRE, 125, e06497
Barraud, O., Besse, S., & Doressoundiram, A. 2023, Low Sulfide Concentration in Mercury's Smooth Plains Inhibits Hollows, SciA, 9, eadd6452
Blewett, D. T., Robinson, M. S., Denevi, B. W., et al. 2009, Multispectral Images of Mercury from the First MESSENGER Flyby: Analysis of Global and Regional Color Trends, EPSL, 285, 272
Blewett, D. T., Lucey, P. G., Hawke, B. R., Ling, G. G., & Robinson, M. S. 1997, A Comparison of Mercurian Reflectance and Spectral Quantities with Those of the Moon, Icar, 129, 217
Blewett, D. T., Chabot, N. L., Denevi, B. W., et al. 2011, Hollows on Mercury: MESSENGER Evidence for Geologically Recent Volatile-Related Activity, Sci, 333, 1856
Blewett, D. T., Vaughan, W. M., Xiao, Z., et al. 2013, Mercury's Hollows: Constraints on Formation and Composition from Analysis of Geological Setting and Spectral Reflectance, JGRE, 118, 1013
Blewett, D. T., Stadermann, A. C., Susorney, H. C., et al. 2016, Analysis of MESSENGER High-Resolution Images of Mercury's Hollows and Implications for Hollow Formation, JGRE, 121, 1798
Blewett, D. T., et al. 2018, Mercury's Hollows, in Mercury: The View After MESSENGER, ed. L. Nittler & B. Anderson (Cambridge Univ. Press), 324
Brunetto, R., & Strazzulla, G. 2005, Elastic Collisions in Ion Irradiation Experiments: A Mechanism for Space Weathering of Silicates, Icar, 179, 265
Burns, R. G. 1993, Mineralogical Applications of Crystal Field Theory (Cambridge Univ. Press)
Cartography and Imaging Sciences Node PDS 2022, MESSENGER MDIS Data Archive, NASA Planetary Data System, doi:10.17189/BDXT-4C65
Clark, R. N., & Roush, T. L. 1984, Reflectance Spectroscopy: Quantitative Analysis Techniques for Remote Sensing Applications, JGR, 89, 6329
Clark, R. N. 1999, Spectroscopy of Rocks and Minerals, and Principles of Spectroscopy, in Manual of Remote Sensing, ed. A. N. Rencz, Vol. 3 (Wiley)

Cloutis, E. A., McCormack, K. A., Kaitlyn, A., et al. 2008, Ultraviolet Spectral Reflectance Properties of Common Planetary Minerals, Icar, 197, 321
Cremonese, G., Capaccioni, F., Capria, M. T., et al. 2020, SIMBIO-SYS: Scientific Cameras and Spectrometer for the BepiColombo Mission, SSRv, 216, 75
De Toffoli, B., Galluzzi, V., Massironi, M., et al. 2024, Hollows on Mercury: A Comprehensive Analysis of Spatial Patterns and Their Relationship to Craters and Structures, E&SS, 11, 10
Denevi, B. W., Robinson, M. S., Solomon, S. C., et al. 2009, The Evolution of Mercury's Crust: A Global Perspective from MESSENGER, Sci, 324, 613
Denevi, B. W., Carolyn, E. M., Meyer, H. M., et al. 2013, The Distribution and Origin of Smooth Plains on Mercury, JGRE, 118, 891
Denevi, B. W., Chabot, N. L., Murchie, S. L., et al. 2018, Calibration, Projection, and Final Image Products of MESSENGER's Mercury Dual Imaging System, SSRv, 214, 52
Deutsch, A. N., Bickel, V. T., & Blewett, D. T. 2025, Hollows on Mercury: Global Classification of Degradation States and Insight into Hollow Evolution, JGRE, 130, e2024JE008747
Domingue, D. L., Chapman, C. R., Killen, R. M., et al. 2014, Mercury's Weather-Beaten Surface: Understanding Mercury in the Context of Lunar and Asteroidal Space Weathering Studies, SSRv, 181, 121
Domingue, D. L., Denevi, B. W., Murchie, S. L., & Hash, C. D. 2016, Application of Multiple Photometric Models to Disk-Resolved Measurements of Mercury's Surface: Insights into Mercury's Regolith Characteristics, Icar, 268, 172
Dyar, M. D., Sklute, E. C., Menzies, O. N., et al. 2009, Spectroscopic Characteristics of Synthetic Olivine: An Integrated Multi-wavelength and Multi-technique Approach, AmMin, 94, 883
Edwards, A. L. 1976, The Correlation Coefficient, An Introduction to Linear Regression and Correlation (W. H. Freeman), 33
Fassett, C. I. 2016, Ames Stereo Pipeline-Derived Digital Terrain Models of Mercury from MESSENGER Stereo Imaging, P&SS, 134, 19
Galiano, A., Capaccioni, F., Filacchione, G., & Carli, C. 2023, Principal Component Analysis Applied on MASCS/MESSENGER Data for the Spectral Investigation of Mercury's Surface, Icar, 401, 115609
Galluzzi, V., Guzzetta, L., Ferranti, L., et al. 2016, Geology of the Victoria Quadrangle (H02), Mercury, JMaps, 12, 227
Goudge, T. A., Head, J. W., Kerber, L., et al. 2014, Global Inventory and Characterization of Pyroclastic Deposits on Mercury: New Insights into Pyroclastic Activity from MESSENGER Orbital Data, JGRE, 119, 635
Hapke, B. 2001, Space Weathering from Mercury to the Asteroid Belt, JGR, 106, 10039
Greenspon, A. S., Hibbitts, C. A., & Dyar, M. D. 2012, LPSC, 43, 2490
Hawkins, S. E., III, Boldt , J. D., Darlington, E. H., et al. 2007, The Mercury Dual Imaging System on the MESSENGER Spacecraft, SSRv, 131, 247
Herzberg, G. 1945, Molecular Spectra and Molecular Structure, Infrared and Raman Spectra of Polyatomic Molecules, Vol. 2 (Van Nostrand, Reinhold)
Hiesinger, H., Helbert, J., Alemanno, G., et al. 2020, Studying the Composition and Mineralogy of the Hermean Surface with the Mercury Radiometer and Thermal Infrared Spectrometer (MERTIS) for the BepiColombo Mission: An Update, SSRv, 216, 110
Izenberg, N. R., Klima, R. L., Murchie, S. L., et al. 2014, The Low-Iron, Reduced Surface of Mercury as Seen in Spectral Reflectance by MESSENGER, Icar, 228, 364
Kerber, L., Head, J. W., Blewett, D. T., et al. 2011, The Global Distribution of Pyroclastic Deposits on Mercury: The View from MESSENGER Flybys 1-3, PSS, 59, 1895
Klima, R. L., Denevi, B. W., Ernst, C. M., Murchie, S. L., & Peplowski, P. N. 2018, Global Distribution and Spectral Properties of Low-Refletance Material on Mercury, GeoRL, 45, 2945
Lucchetti, A., Pajola, M., Galluzzi, V., et al. 2018, Mercury Hollows as Remnants of Original Bedrock Materials and Devolatilization Processes: A Spectral Clustering and Geomorphological Analysis, JGRE, 123, 2365
Lucchetti, A., Pajola, M., Poggiali, G., et al. 2021, Volatiles on Mercury: The Case of Hollows and the Pyroclastic Vent of Tyagaraja Crater, Icar, 370, 114694
Malliband, C. C., Conway, S. J., Rothery, D. A., & Balme, M. R. 2018, Potential Identification of Sublimation-Driven Downslope Mass Movement on Mercury, EPSC, 12, 1001
Melosh, H. J. 1989, Impact Cratering: A Geological Process (Oxford Univ. Press), 245
McClintock, W. E., & Lankton, M. R. 2007, The Mercury Atmospheric and Surface Composition Spectrometer for the MESSENGER Mission, SSRv, 131, 481
McClintock, W. E., Izenberg, N. R., Holsclaw, G. M., et al. 2008, Spectroscopic Observations of Mercury's Surface Reflectance During MESSENGER's First Mercury Flyby, Sci, 321, 62
Munaretto, G., Pajola, M., Lucchetti, A., et al. 2021, Topographic Correction of HiRISE and CaSSIS Images: Validation and Application to Color Observations of Martian Albedo Features, P&SS, 200, 105198
Munaretto, G., Lucchetti, A., Pajola, M., Cremonese, G., & Massironi, M. 2023, Assessing the Spectrophotometric Properties of Mercury's Hollows through Multiangular MESSENGER/MDIS Observations, Icar, 389, 115284
Murchie, S. L., Watters, T. R., Robinson, M. S., et al. 2008, Geology of the Caloris Basin, Mercury: A View from MESSENGER, Sci, 321, 73
Murchie, S. L., Klima, R. L., Denevi, B. W., et al. 2015, Orbital multispectral mapping of Mercury with the MESSENGER Mercury Dual Imaging System: Evidence for the Origins of Plains Units and Low-reflectance Material, Icar, 254, 287
Nittler, L., Frank, E. A., Weider, S. Z., et al. 2020, Global Major-Element Maps of Mercury from Four Years of MESSENGER X-Ray Spectrometer Observations, Icar, 345, 113716
Pajola, M. A., Lucchetti, A., Semenzato, A., et al. 2021, Lermontov Crater on Mercury: Geology, Morphology and Spectral Properties of the Coexisting Hollows and Pyroclastic Deposits, PSS, 195, 105136
Rava, B., & Hapke, B. 1987, An Analysis of the Mariner 10 Color Ratio Map of Mercury, Icar, 71, 397
Robinson, M. S., Murchie, S. L., Blewett, D. T., et al. 2008, Reflectance and Color Variations on Mercury: Regolith Processes and Compositional Heterogeneity, Sci, 321, 66
Schlemm, C. E., Starr, R. D., Ho, G. C., et al. 2007, The X-Ray Spectrometer on the MESSENGER Spacecraft, SSRv, 131, 393
Solomon, S. C., McNutt, R. L., Jr., Gold, R. E., & Domingue, D. L. 2007, MESSENGER Mission Overview, SSRv, 131, 3
Sunshine, J. M., & Pieters, C. M. 1998, Determining the Composition of Olivine from Reflectance Spectroscopy, JGR, 103, 13675
Thomas, R. J., Rothery, D. A., Conway, S. J., & Anand, M. 2014a, Hollows on Mercury: Materials and Mechanisms Involved in Their Formation, Icar, 229, 221
Thomas, R. J., Rothery, D. A., Conway, S. J., & Anand, M. 2014b, Mechanisms of Explosive Volcanism on Mercury: Implications from Its Global Distribution and Morphology, JGRE, 119, 2239
Vilas, F., Domingue, D. L., Helbert, J., et al. 2016, Mineralogical Indicators of Mercury's Hollows Composition in MESSENGER Color Observations, GeoRL, 43, 1450
Warell, J., & Blewett, D. T. 2004, Properties of the Hermean Regolith. V. New Optical Reflectance Spectra, Comparison with Lunar Anorthosites, and Mineralogical Modelling, Icar, 168, 257
Warell, J., Sprague, A. L., Emery, J. P., Kozlowski, R. W. H., & Long, A. 2006, The 0.7 5.3 μm IR Spectra of Mercury and the Moon: Evidence for High-Ca Clinopyroxene on Mercury, Icar, 180, 281
Weider, S. Z., Nittler, L. R., Starr, R. D., McCoy, T. J., & Solomon, S. C. 2014, Variations in the Abundance of Iron on Mercury's Surface from MESSENGER X-Ray Spectrometer Observations, Icar, 235, 170
Zolotov, M. Y. 2011, On the Chemistry of Mantle and Magmatic Volatiles on Mercury, Icar, 212, 24